symmetry

MDPI

Article

Application of Active Attitude Setting via Auto Disturbance Rejection Control in Ground-Based Full-Physical Space Docking Tests

Xiao Zhang [1,2], Yonglin Tian [2,3], Zainan Jiang [1,4,*], Zhigang Xu [2,*], Mingyang Liu [2] and Xinlin Bai [2]

[1] State Key Laboratory of Robotics and Systems, Harbin Institute of Technology, Harbin 150001, China; zhangxiao1@sia.cn
[2] Shenyang Institute of Automation, Chinese Academy of Sciences, Shenyang 110016, China; tianyonglin@sia.cn (Y.T.); liumingyang@sia.cn (M.L.); baixinlin@sia.cn (X.B.)
[3] University of Chinese Academy of Sciences, Beijing 100049, China
[4] Song Jiang Laboratory, Harbin Institute of Technology, Harbin 150001, China
* Correspondence: jiangzainan@hit.edu.cn (Z.J.); zgxu@sia.cn (Z.X.)

Abstract

Ground-based full-physical experiments for space rendezvous and docking serve as a critical step in verifying the reliability of docking technology. The high-precision active attitude setting of spacecraft simulators represents a key technology for ground-based full-physical experiments. In order to satisfy the requirement for high-precision attitude control in these experiments, this paper proposes an enhanced method based on auto disturbance rejection control (ADRC). This paper addresses the limitations of traditional deadband–hysteresis relay controllers, which exhibit low steady-state accuracy and insufficient disturbance rejection capability. This approach employs a nonlinear extended state observer (NESO) to estimate and compensate for total system disturbances in real time. Concurrently, it incorporates an adaptive mechanism for deadband and hysteresis parameters, dynamically adjusting controller parameters based on disturbance estimates and attitude errors. This overcomes the trade-off between accuracy and power consumption that is inherent in fixed-parameter controllers. Furthermore, the method incorporates a nonlinear tracking differentiator (NTD) to schedule transitions, enabling rapid attitude settling without overshoot. The stability analysis demonstrates that the proposed controller achieves local asymptotic stability and global uniformly bounded convergence. The simulation results demonstrate that under three typical operating conditions (conventional attitude setting, pre-separation connector stabilisation, and docking initial condition establishment), the steady-state attitude error remains within $\pm 0.01^{\circ}$, with convergence times under 3 s and no overshoot. These results closely match ground test data. This approach has been demonstrated to enhance the engineering applicability of the control system while ensuring high precision and robust performance.

Keywords: active attitude setting; auto disturbance rejection control; nonlinear extended state observer; nonlinear tracking differentiator; deadband–hysteresis control; ground-based full-physical experiment; dynamic parameter adaptation

Check for updates

Academic Editor: Theodore E. Simos

Received: 14 December 2025
Revised: 12 January 2026
Accepted: 15 January 2026
Published: 16 January 2026

Copyright: © 2026 by the authors. Licensee MDPI, Basel, Switzerland. This article is an open access article distributed under the terms and conditions of the Creative Commons Attribution (CC BY) license.

1. Introduction

Space rendezvous and docking is a core enabling technology for major space missions, including space station assembly, in-orbit refuelling of spacecraft, and satellite repair. The

precision and reliability of its control determine the success of in-orbit operations and the expansion of space application capabilities. Through its manned space programmes, including Apollo, Skylab, satellite servicing missions using the Space Shuttle, Shuttle–Mir docking operations, the International Space Station program, and the Orion spacecraft program, the United States has continuously researched, developed, refined, and perfected rendezvous and docking technology. In 1975, the Apollo spacecraft successfully rendezvoused and docked with the Soviet Soyuz spacecraft, marking the first docking between U.S. and Soviet spacecraft. This mission employed a novel heterogeneous peripheral docking mechanism [1]. However, space rendezvous and docking missions are typically characterised by extreme complexity, high risk, and significant costs. This makes it impractical to rely solely on in-orbit testing for technology validation. Therefore, ground-based, full-physical experiments that can reproduce the space environment and the dynamic characteristics of rendezvous and docking with high fidelity have become an indispensable component of the research and development process for rendezvous and docking technology [2]. China has also conducted systematic exploration in this field. In 2008, the Shanghai Institute of Space Systems Engineering conducted a research study on the docking and separation of space vehicles [3]. This research included both simulation analysis and ground simulation tests. The study discussed the analogy relationship between the space separation process of two vehicles at the moment of separation and the ground simulation test process. It also compared the motion characteristics of two spacecraft during separation under both ground and space zero-gravity conditions. This was based on multiple operational conditions provided by ground tests. Finally, the study discussed the influence of principal errors introduced by the ground five-degree-of-freedom docking separation air-bearing platform when simulating the actual separation of two spacecraft in space. In 2014, the China Academy of Space Technology developed a series of system-level integrated tests to rapidly master rendezvous and docking technology within a limited number of flight tests. These tests combined partial and full-scale simulations, single-environment and comprehensive-environment scenarios, and experimental verification with simulation methods. These methods were based on a thorough analysis and integration of ground validation requirements [4]. These efforts illustrate that ground-based full-physical experiments not only validate the performance and effectiveness of core components and control algorithms but also provide a cost-effective and secure platform for assessing the reliability of system integration.

This study aims to conduct ground-based full-physical experiments using a space docking performance buffer test bench—the core of the ground verification system. The test bench integrates an air-bearing platform, a five-degree-of-freedom spacecraft mock-up, and a multi-dimensional force measurement and real-time control system, designed to replicate the entire docking and separation process under space microgravity conditions. Its core consists of two spacecraft simulators (active tracking unit and passive target unit), mounted on an air-bearing platform to achieve in-plane three-degree-of-freedom drift motion. The simulators are also placed on a two-dimensional turntable, the attitude of which is precisely controlled by an active control system. The test bench coordinates the relative orientation between the turntable and the air-bearing platform to simulate a continuous sequence: initial approach, collision, capture, buffered retraction, and final separation reset. Throughout the process, real-time data on collision forces, torques, and relative orientation are collected, providing critical experimental support for evaluating the docking mechanism's buffer damping performance, energy absorption efficiency, and dynamic coupling effects.

Despite significant advances in space docking research and full-physical experiments regarding docking mechanism design, dynamic modelling, and six-degree-of-freedom

simulator control [5,6], a critical yet often overlooked aspect of experimental systems is the active attitude setting of the aforementioned tracker simulators. In ground-based full-physical experimental systems, achieving high-precision simulation of in-orbit space docking processes requires spacecraft mock-ups to actively and accurately set and maintain specific attitudes according to experimental procedures. This active attitude setting has been demonstrated to serve as the critical link between experimental commands and physical execution. The precision of the measurement directly impacts the accuracy of the relative position and attitude measurements between the target and the tracker. This, in turn, determines the validity of the experimental data and the credibility of the technical verification results. In order to simulate normal in-orbit operations, stabilise the connector prior to separation, or establish initial docking conditions, the attitude control system must rapidly drive the mock-up to target attitudes without overshoot, whilst maintaining stability. Furthermore, it is imperative that the system demonstrates an ability to withstand minor disturbances within the experimental environment. In order to achieve the optimal acquisition of attitude, it is necessary to strike a balance between convergence speed, steady-state accuracy, and robustness. In order to achieve these objectives, scholars worldwide have conducted extensive research. Zhao et al. proposed a flexible model based on a virtual repulsive potential field, utilising the technique of deep reinforcement learning. Through static multi-constraint pre-planning and dynamic adjustment of virtual modal parameters via DRL agent training, the desired dynamic control of robotic milling attitudes was achieved, thus establishing a foundation for dynamic milling of large, high-curvature parts in narrow spaces [7]. Yan et al. proposed a global trajectory tracking controller for vehicle-like mobile robots. The design of this controller is based on the original tracking error equation, thus avoiding singularities and possessing a globally attractive domain. It has been demonstrated that the system can be extended to perform pose-stable control tasks incorporating obstacle avoidance, with its convergence rigorously proven via contradiction and Barbalat's lemma. This approach presents a novel methodology for mobile robot motion control that is both singularity-free and globally effective, a claim substantiated by experimental validation [8]. Khan et al. reviewed research progress in active attitude control for microsatellites, encompassing CubeSat applications, typical architectures combining magnetostatic and momentum wheel systems, key challenges, and the potential application value of embedded planar magnetorotoric torquers [9]. In ground-based full-physical experiments, satellite simulators are required to maintain stable attitudes for extended periods or rapidly adjust to preset configurations according to experimental protocols. This imposes stringent demands on attitude control technology: high steady-state accuracy to ensure consistent experimental conditions, robust disturbance rejection to suppress environmental disturbances such as air resistance and ground vibrations, and rapid response capabilities to meet experimental time constraints.

The majority of studies either presuppose that the attitude of the mock-up is already in an ideal state or focus exclusively on the relative attitude at the instant of docking. A paucity of in-depth exploration of active, high-precision attitude setting techniques during scenarios such as the experimental preparation phase, specific dynamic processes, and critical pre-mission periods is evident [10]. In the ground-based full-physical experiments of spatial docking performance underpinning this research, the typical workflow primarily encompasses two core operations: docking and undocking. In order to replicate and evaluate the performance of these operations with a high degree of precision, it is necessary to maintain the attitude of spacecraft mock-ups at different stages of the experiment with great accuracy. The present study focuses on three experimental processes with explicit requirements for active attitude control, as illustrated in Figure 1, alongside corresponding research content:

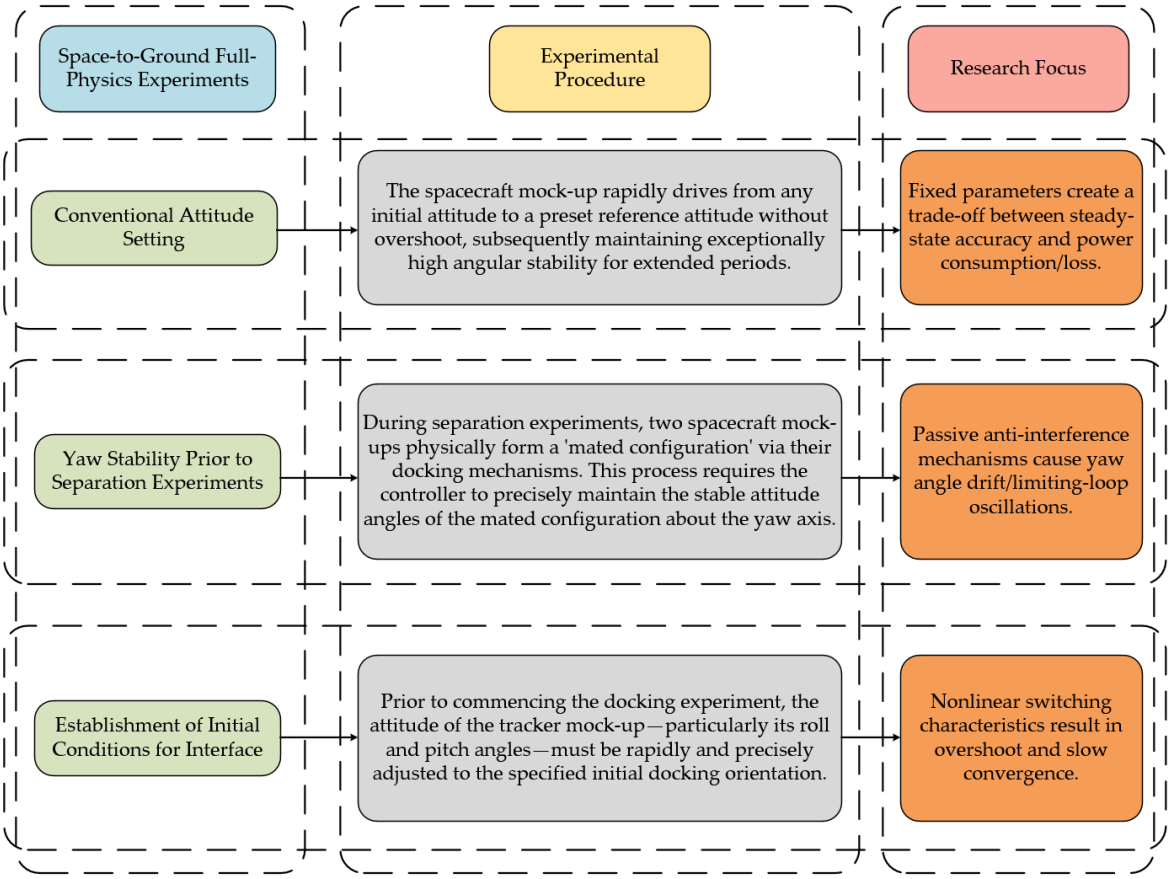


Figure 1. The Entire Physical Experiment Process for Space-to-Ground Docking and Its Research Challenges.

In order to address this challenge, the present paper introduces a theory of self-disturbance-rejection control, based on traditional deadband–hysteresis controllers. This theoretical framework allows for systematic architectural innovation and theoretical refinement.

Firstly, a dynamic adaptive mechanism for deadband–hysteresis parameters was proposed, based on disturbance estimation. This mechanism achieved intelligent matching between controller parameters and system operating conditions. In traditional controllers, deadband and hysteresis parameters are fixed values, resulting in a trade-off between precision and power consumption when confronted with varying disturbance intensities and dynamic requirements. Addressing the issue of adaptive parameter tuning, researchers have conducted relevant studies for different application scenarios. For instance, Zhang et al. addressed the performance degradation of parameter-adaptive differential evolution algorithms in noisy environments due to unreliable fitness comparisons. The proposed methodology is centred upon a parameter adaptation technique that is assisted by the utilisation of fuzzy logic systems. This approach is predicated on the comprehensive estimation of parameters through the utilisation of search feedback and the correlation between the objective and solution spaces. This, in turn, serves to enhance the performance of optimisation in conditions that are characterised by noise. The efficacy of this approach is evidenced by its superior performance in comparison to conventional methods that are predicated exclusively on fitness comparisons and other evolutionary algorithms [11]. Reza et al. addressed the issue of performance degradation in pre-trained multimodal networks during testing due to missing modalities. The researchers proposed an intermediate feature modulation adaptation method requiring only minimal parameters. This approach enhances robustness by compensating for missing modalities, is applicable to various

modality combinations and tasks, and outperforms existing robust multimodal learning methods for missing modalities [12]. Faraji et al. proposed an ADRC based on the deep deterministic policy gradient (DDPG) for deep brain stimulation therapy in Parkinson's disease, with the objective of targeting the stimulation of the subthalamic nucleus and medial globus pallidus. The ADRC coefficients were treated as target parameters, which were dynamically designed via a DDPG neural network, thereby enabling adaptive parameter optimisation. This approach effectively reduced electric field intensity, side effects, and hand tremors, with simulation and hardware-in-the-loop (HIL) validation confirming the efficacy of adaptive parameter tuning [13]. Peng et al. addressed the challenges associated with yarn tension control in knitted underwear machines by designing a fuzzy sliding mode-based adaptive ADRC algorithm tension control system. This system dynamically adjusts feeder motor parameters through real-time tension detection, achieving adaptive optimisation of tension control parameters and significantly enhancing tension stability across different fabrics and process conditions [14].

Secondly, a cooperative control architecture based on ADRC was constructed, thereby achieving a fundamental shift from passive response to auto disturbance rejection. The fundamental premise of ADRC entails the real-time estimation and compensation of total system disturbances through the utilisation of an extended state observer (ESO). Since its systematic introduction [15], this concept has demonstrated robust performance across multiple domains [16]. A research study was conducted in order to investigate the intrinsic connection between ADRC and standard PI/PID controllers. The aim was to establish formal equivalence conditions between the two. A proposed methodology for transitioning from PI/PID to error-based ADRC was presented, achieving conversion from one degree of freedom (DOF) to two DOF while preserving the standard 2DOF PI/PID structure. This enables ADRC to combine strong robustness with a controller form commonly used in industry, thereby promoting its industrial application. The theoretical effectiveness of the proposed model was validated through the implementation of frequency domain tests [17]. In order to address the challenges of underwater navigation and control encountered by amphibious multi-rotor vehicles, Li et al. have designed a cascaded ADRC motion controller and employed a particle swarm optimisation algorithm for the purpose of rapid parameter tuning. Significant improvements were achieved by deriving kinematic and dynamic equations, analysing hydrodynamics, and designing position and attitude ADRC controllers. The simulation results demonstrate that, in comparison with PID and sliding mode controllers, the ADRC exhibits accelerated response, augmented disturbance rejection, and enhanced robustness in the presence of external strong disturbances, thereby satisfying the control requirements of complex underwater environments [18]. The ultimate value of high-performance attitude control algorithms lies in their reliable physical implementation. In practical engineering applications, whether in ground-based full-physical experiments using spacecraft simulators or in micro-satellites operating in orbit, the core of the control system is typically based on real-time embedded computing platforms. While these platforms provide substantial computational power, they also face stringent resource constraints, including limited processor clock speeds, memory capacity, and deterministic interrupt response requirements. Consequently, evaluating control algorithms extends beyond theoretical performance to encompass computational efficiency, code complexity, and real-time reliability within embedded environments. For instance, Zhang et al. successfully implemented ADRC-based sensorless permanent magnet synchronous motor control on an STM32F4 microcontroller, demonstrating the feasibility of implementing complex observation and control logic using ADRC algorithm structures on typical embedded hardware [19]. The theoretical framework and empirical data demonstrating the

application of the ADRC method to address interference mitigation issues, as outlined in the aforementioned research, are presented in Table 1.

Table 1. Core Methods and Specific Data in Research Employing the ADRC Approach to Address Interference Resistance Issues.

Core Methodology	Key Experimental Data			
Establish an equivalence relationship between PID and ADRC, representing the error-based ADRC scheme as a standard 1DOF/2DOF controller.	Performance indicators	PI/PID		ADRC
	Disturbance suppression level (dB)	−40 (1 rad/s, second-order system)		60 (1 rad/s, second-order system)
	Disturbance recovery time (s)	2.5 (First-order system)		1.8 (First-order system)
An anti-interference control (ADRC) approach was employed to construct a series-connected motion controller, with particle swarm optimisation (PSO) introduced for rapid parameter tuning.	Performance indicators	PID	SMC	ADRC
	Trajectory deviation (m)	0.12	0.15	0.08
	Recovery time (s)	2	3	1
	Attitude angle fluctuation range (°)	[−1.5°, 1.5°]	[−3°, 3°]	[−1.6°, 1.6°]
	Recovery time (s)	2	3	1
Design of a Sensorless ADRC Vector Control Method Based on the Luenberger Observer for Permanent Magnet Synchronous Motors.	Performance indicators	PI		ADRC
	Comparison of Speed Errors Under Load Disturbance	−15~7.5 r/min		−18~−3 r/min
	Torque Fluctuation Comparison	3.5~5.5 Nm		4~4.5 Nm
	Speed steady-state fluctuation	850~880 r/min		880~915 r/min

Thirdly, an NTD was introduced to plan command transitions without overshoot, thereby resolving the dynamic trade-off in rapid attitude manoeuvres. Their research on command transition processes and overshoot suppression mechanisms provides a theoretical framework for addressing the classic contradiction between rapid response and overshoot-free control. In addition, it provides a critical technological foundation for enhancing operational safety and reliability in hazardous missions within practical engineering applications. For instance, Li et al. proposed an integrated flow compensation backstepping controller to address overshoot issues in high-frequency electrohydraulic systems caused by high-response position tracking, as well as the dynamic performance trade-offs resulting from conventional over-damping or feedback coefficient reduction strategies. This controller resolves the contradiction between overshoot suppression and response speed in traditional methods by synthesising nonlinear friction, delay, and dead-band factors, while simultaneously converting flow error and delay compensation in real time [20]. In their seminal paper, Zhang et al. proposed a series of Kirigami structures with the aim of addressing the challenge of balancing operational range and overshoot in flexible strain sensors for large deformation detection. This strategy employs a domino effect to adapt to high-curvature deformations, thereby expanding the sensor's operational range while reducing overshoot. This provides an effective solution balancing operational range and overshoot for large deformation scenarios [21]. Liu and Xiong proposed a multi-objective optimisation control method based on an overlimit suppression strategy to address ammonia nitrogen and total nitrogen exceedances in wastewater treatment. The establishment of a water quality prediction model was achieved, and this was then combined with a dynamic multi-objective evolutionary algorithm. The purpose of this combination was to optimise setpoints and implement tracking control. During exceedance events, the external recirculation, carbon sources, and dissolved oxygen were regulated, and secondary optimisation was performed to reduce nitrate nitrogen levels. This approach led to a substantial reduction in both exceedance duration and energy consumption, thereby effectively suppressing water quality exceedances [22].

The structure of this paper is as follows: Section 2 of this study establishes a decoupled model of the attitude dynamics for spacecraft mock-ups. This provides a theoretical foundation for controller design. Section 3: This section undertakes a systematic analysis of the phase plane characteristics of traditional dead-zone–hysteresis controllers. The analysis

reveals the inherent limitations of these controllers with regard to steady-state accuracy and disturbance rejection capability. Section 4: This section puts forward a proposal for an enhanced ADRC-based solution. The design of NTD, NESO, and dynamic parameter adaptation mechanisms enables auto disturbance compensation and overshoot-free control, as evidenced by stability analysis. In Section 5, the validation of simulations is conducted under three typical operating conditions. A quantitative evaluation of the engineering effectiveness of the improved algorithm is provided by comparing it with ground test data. In conclusion, Section 6 offers a comprehensive summary of the research findings, highlighting the limitations of the study and outlining potential avenues for future research.

2. Establishment of Posture Kinematic Models

The attitude dynamics model provides the theoretical foundation for the design and performance analysis of spacecraft attitude control algorithms. The present section is concerned with the attitude control requirements of spacecraft simulators in ground-based full-physical experiments for space docking. It establishes a complete set of attitude dynamics equations based on classical mechanics theory. This objective is realised through the delineation of inertial coordinate systems and the subsequent derivation of the moment of momentum theorem. In consideration of the prevailing engineering characteristic, which dictates that "attitude angular velocity is significantly smaller than orbital angular velocity", a decoupling and simplification of the coupled three-axis dynamics model was undertaken. This approach culminated in the derivation of an independent pitch channel control model. The model under discussion explicitly defines the quantitative mapping relationship between the control input torque, the external disturbance torque, and the attitude angular acceleration. This simplified model preserves the core dynamic characteristics of the controlled object while eliminating complex coupling terms and reducing computational redundancy. The model provides an accurate and efficient mathematical foundation for the subsequent design, analysis and validation of controllers.

The motion of an object is invariably relative to a particular reference coordinate system, which is associated with specific objects or celestial bodies. In the event of Newton's first law being valid within a coordinate system, said system is designated as an inertial (coordinate) system. It is hypothesised that the system under consideration consists of N particles, with the corresponding density function expressed as $\rho_i (i = 1, 2, \cdots, N)$. The mass of particle ρ_i is denoted as m_i, and the total mass is given by $M = \sum_{i=1}^{N} m_i$. The reference coordinate system $Oxyz$ is defined as an inertial frame. The position vector from point O to ρ_i is denoted as $\mathbf{r}_i$, and the velocity vector of ρ_i is denoted as $\mathbf{v}_i$. The centre of mass of the system is denoted as C, the position vector from O to C is $\mathbf{r}_C$, and the velocity of C is $\mathbf{v}_C$. The resultant external force acting on ρ_i is denoted $\mathbf{F}_i$. The total momentum of the system is defined as $\mathbf{Q} = \sum_{i=1}^{N} m_i v_i$. In accordance with Newton's laws of motion, the subsequent fundamental theorems of dynamics may be deduced.

The reference point, denoted by the symbol O_S, can be either fixed or non-fixed in the coordinate system $Oxyz$. The vector from point O to point O_S is denoted by $\mathbf{r}_S$, the velocity of point O_S is denoted by $\mathbf{v}_S$, and the vector from point O_S to point ρ_i is denoted by $\mathbf{r}_{Si}$. The quantity $H_S = \sum_{i=1}^{N} \mathbf{r}_{Si} \times m_i v_i$ is defined as the moment of momentum (angular momentum) of the system with respect to point O_S. From this, the following equation can be derived:

$$\frac{d}{dt}\mathbf{H}_S = \sum_{i=1}^{N} \mathbf{r}_{Si} \times \mathbf{F}_i - \mathbf{v}_S \times \mathbf{Q} \tag{1}$$

Equation (1) is the momentum theorem: the differential with respect to time of the angular momentum of a system about a reference point O_S is equal to the sum of the moment of external forces acting on the system about point O_S and the vector product of the velocity vector of the reference point and the momentum of the system.

When the reference point, denoted by the symbol O_S, is designated as the centre of mass, denoted by the symbol C, of the system under consideration, this reference point assumes particular significance in practical applications. In this particular instance $\mathbf{v}_S \times \mathbf{Q} = 0$, so we have the following:

$$\frac{d\mathbf{H}_C}{dt} = \sum_{i=1}^{N} \mathbf{r}_{Ci} \times \mathbf{F}_i \tag{2}$$

Equation (2) demonstrates that when the system's centre of mass C, is selected as the reference point, the moment of momentum theorem assumes the same concise form as when a fixed point is adopted as the reference point. The centroidal coordinate system is thus employed to investigate the rotational motion of objects.

Consider a spacecraft simulator with its centre of mass at C. A body coordinate system, denoted $Cxyz$, is established (rigidly attached to the simulator). The inertia matrix of the simulator is represented by $\mathbf{I}$ in the $Cxyz$ coordinate system. The projections of the simulator's angular velocity vector onto the axes of $Cxyz$ are denoted by ω_x, ω_y, ω_z. By defining $\boldsymbol{\omega} = \begin{pmatrix} \omega_x & \omega_y & \omega_z \end{pmatrix}^{\mathrm{T}}$, it can be demonstrated that the components of the moment of momentum $\mathbf{H}_C$ of the simulator relative to its centre of mass C, in the $Cxyz$ coordinate system can be expressed as follows:

$$\mathbf{H}_C = \begin{pmatrix} H_{Cx} & H_{Cy} & H_{Cz} \end{pmatrix}^{\mathrm{T}} = \mathbf{I} \begin{pmatrix} \omega_x & \omega_y & \omega_z \end{pmatrix}^{\mathrm{T}} \tag{3}$$

The external torque applied to the simulated component is denoted $\mathbf{T}$. In accordance with the theorem of angular momentum, the following equation is established:

$$\frac{d}{dt}\mathbf{H}_C = \mathbf{T} \tag{4}$$

It can be posited that $\mathbf{H}_C$ is the relative micro-business within $Cxyz$, denoted as $\dot{\mathbf{H}}_C$:

$$\dot{\mathbf{H}}_C + \boldsymbol{\omega} \times \mathbf{H}_C = \mathbf{T} \tag{5}$$

In this context, $\boldsymbol{\omega}$ denotes the angular velocity vector of $Cxyz$. Expressing Equation (4) in matrix form results in the following:

$$(\mathbf{I}\boldsymbol{\omega})^{\bullet} + \tilde{\boldsymbol{\omega}} \times \mathbf{I}\boldsymbol{\omega} = \mathbf{T} \tag{6}$$

where

$$\tilde{\boldsymbol{\omega}} = \begin{bmatrix} 0 & -\omega_z & \omega_y \\ \omega_z & 0 & -\omega_x \\ -\omega_y & \omega_x & 0 \end{bmatrix} \quad \mathbf{T} = \begin{bmatrix} T_x \\ T_y \\ T_z \end{bmatrix} \quad \boldsymbol{\omega} = \begin{pmatrix} \omega_x & \omega_y & \omega_z \end{pmatrix}^{\mathrm{T}} \tag{7}$$

It can be posited that T_x, T_y, T_z is the component of $\mathbf{T}$ in $Cxyz$.

Since $\mathbf{I}$ is immutable in $Cxyz$, we have the following:

$$\mathbf{I}\dot{\boldsymbol{\omega}} + \tilde{\boldsymbol{\omega}} \times \mathbf{I}\boldsymbol{\omega} = \mathbf{T} \tag{8}$$

Specifically, taking $Cxyz$ as the principal inertia coordinate system, we have

$$\mathbf{I} = \begin{bmatrix} I_x & 0 & 0 \\ 0 & I_y & 0 \\ 0 & 0 & I_z \end{bmatrix} \tag{9}$$

If the analogue component is treated as a rigid body with three attitude angles (roll, pitch and yaw) denoted θ, φ and ψ, respectively, then the following attitude dynamics equations apply under conditions of very small attitude angular velocities:

$$\left.\begin{array}{c} I_x\ddot{\theta} + (I_z - I_y)\omega_0\dot{\psi} = T_x \\ I_y\ddot{\varphi} = T_y \\ I_z\ddot{\psi} + (I_y - I_x)\omega_0\dot{\theta} = T_z \end{array}\right\} \tag{10}$$

In this equation, T_x, T_y, T_z denote the three components of the external torque in the body coordinate system of the simulator, I_x, I_y, I_z represent the three principal moments of inertia of the satellite simulator, and ω_0 is the orbital angular velocity of the simulator.

The attitude angular velocity of the simulator is generally much smaller than ω_0. Therefore, the terms containing $\omega_0\dot{\psi}$ and $\omega_0\dot{\theta}$ in the above equation can be neglected. Consequently, the dynamical equations of the three axes can be fully decoupled, allowing for the independent design of controllers.

Taking the roll channel as an example, the dynamical equation is given by

$$\begin{array}{l} I_x\ddot{\theta} = T_x \\ T_x = T_{\mathrm{cx}} + T_{\mathrm{dx}} \end{array} \tag{11}$$

In this equation, T_{cx} and T_{dx} denote the control input torque and the external disturbance torque of the roll axis, respectively. The system is designed such that $T_{\mathrm{cx}} \gg T_{\mathrm{dx}}$, in which case the above equation can be rewritten as follows:

$$\ddot{\varphi} = a_{\mathrm{c}} + a_{\mathrm{d}} \tag{12}$$

In this expression, a_{c} and a_{d} represent the control angular acceleration and the disturbance angular acceleration, respectively. a_{c} is a constant whose sign and duration are determined by the nonlinear switching controller.

To more intuitively demonstrate the spatial correlation and interaction between each physical quantity and the rigid body of the spacecraft simulator, we have constructed a physical schematic diagram of the attitude dynamics of the simulator, following the definition of the body coordinate system and the roll, pitch and yaw attitude angles. This is shown in Figure 2:

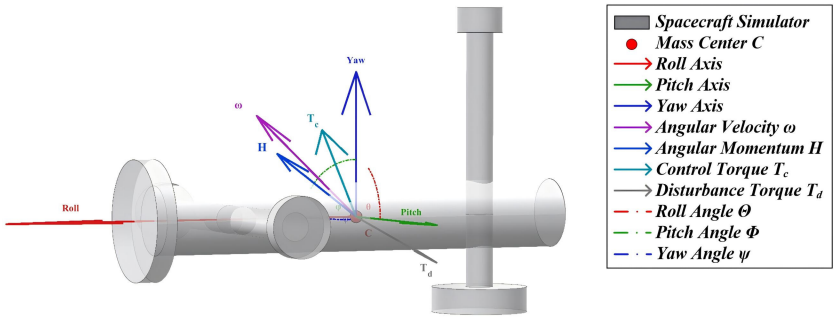


Figure 2. Physical schematic for attitude setting of spacecraft simulator.

This diagram simplifies the analogue component body while clearly integrating the core modelling elements. These are the body coordinate system (with the simulator's centre of mass, C, as the origin), the roll angle, θ, the pitch angle, ϕ, and the yaw angle, ψ (which characterise the attitude state), as well as the angular momentum, $\mathbf{H}_C$, the control torque, T_c, and the disturbance torque, T_d, which drive attitude changes.

3. Dead Zone—Design of Hysteresis Relay Controllers and Phase Plane Characteristics Analysis

Based on the simplified attitude dynamics model of the spacecraft mock-up presented in Section 2, the design of the controller must address two key challenges. Firstly, the spacecraft mock-up has a low angular rate and is susceptible to minor disturbances. This requires the avoidance of actuator wear caused by the controller's high-frequency switching. Secondly, the presence of external disturbance torques necessitates robust disturbance rejection from the controller. The deadband–hysteresis relay controller is well-suited to this scenario due to its inherent properties: deadband filtering mitigates minor errors and hysteresis suppresses high-frequency chatter. This section will first complete the mathematical modelling and parameter definition of this controller. It will then analyse its motion trajectories and stability under disturbance-free, weakly disturbed and strongly disturbed conditions using the phase plane method. Finally, the operational principles and limitations of the controller will be clarified.

3.1. Controller Design

The mathematical description of the nonlinear switch controlling the a_c symbol and duration for the simplified attitude dynamics model is as follows:

$$u_c = \begin{cases} 1 & \varepsilon \geq \theta_D \\ 1 & \varepsilon > (1-h)\theta_D, \dot{\varepsilon} < 0 \\ 0 & -(1-h)\theta_D \leq \varepsilon < \theta_D, \dot{\varepsilon} > 0 \\ 0 & -\theta_D < \varepsilon \leq (1-h)\theta_D, \dot{\varepsilon} < 0 \\ -1 & \varepsilon \leq -\theta_D \\ -1 & \varepsilon < -(1-h)\theta_D, \dot{\varepsilon} > 0 \end{cases} \tag{13}$$

$$\varepsilon = \theta - y \tag{14}$$

where u_c denotes the command signal output by the controller; ε denotes the input signal to the Schmitt trigger, which is also the error signal; θ denotes the reference input signal; y denotes the measurement signal output by the attitude sensor; θ_D denotes the deadband; h denotes the hysteresis coefficient.

This nonlinear switching controller is a nonlinear system with dead-zone relay characteristics, as shown in Figure 3. The hysteresis coefficient h is a dimensionless parameter that typically ranges from 0 to 1 and defines the width of the hysteresis loop. It introduces a hysteresis interval, $h\theta_D$, when the error changes direction. This reduces the controller's frequent actions near the switching point, which directly influences system stability and response speed. For example, when the error increases to a specific threshold, the controller does not switch immediately. Instead, the error must exceed the threshold by a certain proportion to trigger switching. Additionally, the controller adopts distinct switching thresholds for increasing and decreasing errors, forming an asymmetric switching logic (also known as the hysteresis effect). For example, when the error rises from low to high, a higher threshold, θ_D, is required to activate the controller, whereas when the error drops

from high to low, a lower threshold, $(1-h)\theta_D$, is required to deactivate the controller. For such nonlinear switches, the phase-plane method is generally employed for analysis.

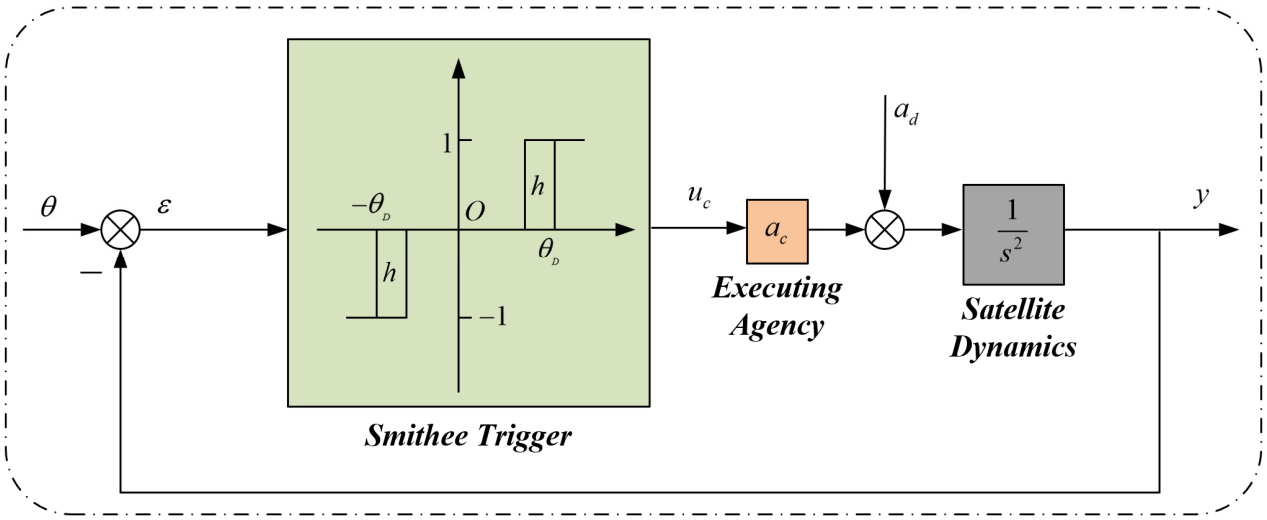


Figure 3. Traditional dead zone—hysteresis relay controller block diagram.

3.2. Phase Plane Method

The phase plane method is an effective approach for studying nonlinear vibrations [23]. For example, the general form of the dynamic equation for the free vibration of a single-degree-of-freedom system is

$$\ddot{x} + f(x, \dot{x}) = 0 \tag{15}$$

In the equation, x and $\dot{x}$ denote the displacement and velocity of the particle, respectively, while $f(x, \dot{x})$ is a linear or non-linear function of x and $\dot{x}$. If we take

$$y = \dot{x} \tag{16}$$

we can obtain the following:

$$\frac{dy}{dx} = \frac{-f(x, y)}{y} \tag{17}$$

At this point, if a coordinate plane Oxy is constructed using x and y as rectangular coordinates (as shown in Figure 4), this plane is referred to as the phase plane of the system. The system's instantaneous motion state (x, y) corresponds to a point on Oxy (called a phase point). As each distinct point on the phase plane corresponds to a unique state of the system, the system's variation in motion state can be represented by the movement of a phase point on the phase plane. The path traced by the phase point during its movement is defined as the phase trajectory, and different phase trajectories within the phase plane never intersect. As time progresses, the phase point moves from left to right in the upper half-plane $(y > 0)$ and from right to left in the lower half-plane $(y < 0)$. On the horizontal axis, the phase trajectory is orthogonal to the axis $y = 0, dy/dx \to \infty$. The key to analysing the motion properties of the system lies in the characteristics of phase trajectories, primarily their direction and behavioural features. For stability analysis, the quantitative variations or laws of the phase point's motion along the trajectory are less important. Thus, the phase-plane method is a qualitative or geometric approach: it maps all possible motions of a vibration system onto the phase plane, providing a "portrait" of the system's motion properties.

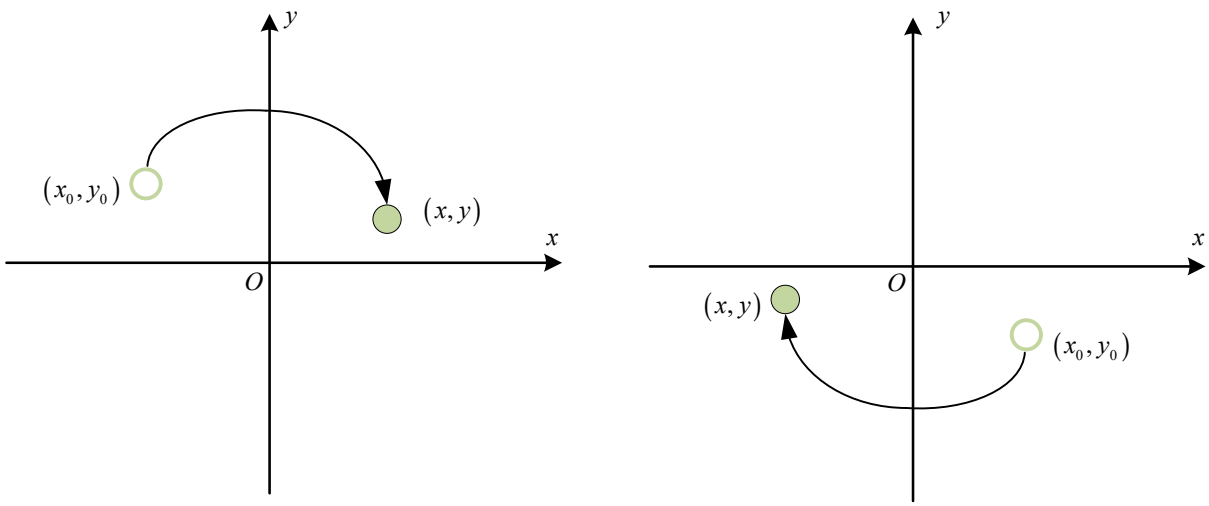


Figure 4. Phase plane, phase point, and phase trajectory.

A particular point on the phase plane, where both the numerator and denominator on the right-hand side of the vibration equation become zero, is designated a singular point of the phase trajectory. Consequently, all singular points are located on the horizontal axis. At a specific point, denoted by the symbol $\dot{x} = \dot{y} = 0$, it can be deduced that the velocity and acceleration of the system are both zero. From a physical perspective, this corresponds to a "static" equilibrium state of the system, signifying that the singular point is indeed an equilibrium point. The equilibrium state (or singular point) of the system can be classified as either stable or unstable. Stable singular points include stable foci and centres. In contrast, unstable singular points include saddle points.

3.3. Analysis of System Disturbance-Free

Firstly, the state variables for the deadband–hysteresis relay controller must be defined, with the error and its derivative selected as the phase plane state variables:

$$\begin{aligned} \varepsilon &= \theta - y \\ \ddot{\varepsilon} &= -\ddot{y} = -(a_c \cdot u_c + a_d) \end{aligned} \tag{18}$$

Depending on the existence of perturbations, two scenarios are analysed. In the absence of perturbations, the dynamic equation is

$$\ddot{\varepsilon} = -a_c \cdot u_c \tag{19}$$

In this context, it is important to note that the constant, denoted by the symbol a_c, remains constant. The phase plane of the system is divided into three regions: the positive saturation region, the negative saturation region, and the dead zone. In the event of $\varepsilon \geq \theta_D$, or $\varepsilon > (1-h)\theta_D$ (with $\dot{\varepsilon} < 0$), the system operates in the positive saturation region of the phase plane (where $u_c = 1$) and the dynamic equation is expressed as follows:

$$\ddot{\varepsilon} = -a_c \tag{20}$$

In the upper half-plane, the phase trajectory moves clockwise with a constant slope of $-a_c$ and the error ε increases accordingly. In the lower half-plane, the phase trajectory also moves clockwise with a constant slope of $-a_c$, but the error ε gradually decreases.

When $\varepsilon \leq -\theta_D$, or when $\varepsilon < -(1-h)\theta_D$ (with $\dot{\varepsilon} > 0$), the system operates in the negative saturation region of the phase plane (where $u_c = -1$), and the dynamic equation is expressed as follows:

$$\ddot{\varepsilon} = a_c \tag{21}$$

In the lower half-plane, the phase trajectory moves clockwise with a constant slope of a_c (accompanying the change of ε); subsequently, in the upper half-plane, it continues to move clockwise with the constant slope of a_c, and the error ε gradually decreases. When $-(1-h)\theta_D \leq \varepsilon < \theta_D$ (with $\dot{\varepsilon} > 0$), or when $-\theta_D < \varepsilon \leq (1-h)\theta_D$ (with $\dot{\varepsilon} < 0$), the system is in the dead zone of the phase plane (where $u_c = 0$), and the controller ceases to act. The corresponding dynamic equation is

$$\ddot{\varepsilon} = 0 \tag{22}$$

The deadband threshold is $\theta_D = 1$, the hysteresis coefficient is set to 0.2, respectively, and the control acceleration amplitude is $a_c = 0.5$. Figure 5 shows the phase trajectory diagram of the system under no disturbance:

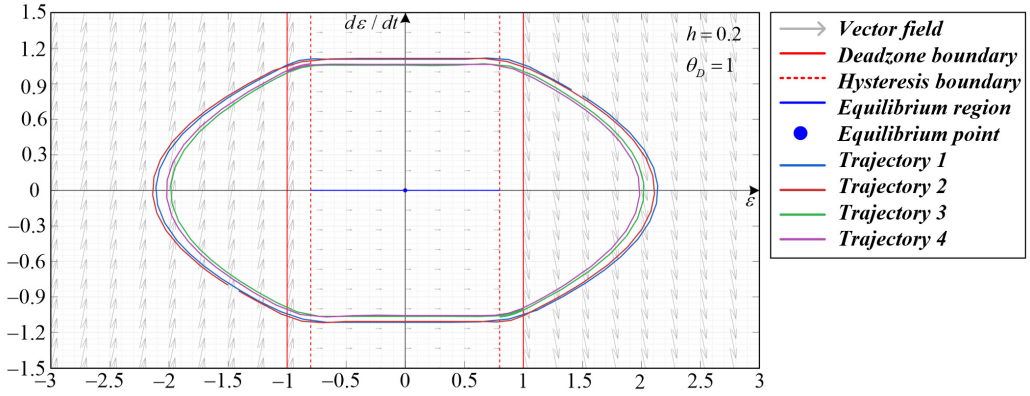


Figure 5. Phase trajectory diagram of the system under no disturbance.

In the absence of significant disturbances, the deadband–hysteresis controller uses a 'saturation zone acceleration/deceleration—hysteresis transition—deadband drift' switching logic to make the attitude error oscillate periodically within a finite range. This process ultimately causes it to converge towards the equilibrium region. This periodic oscillation is a compromise between 'suppressing high-frequency switching' and 'deadband static error': the deadband prevents unnecessary control during minor errors, while the hysteresis eliminates high-frequency jitter. However, this comes at the cost of achieving 'zero static error', as the error is limited to a preset range. Furthermore, the influence of h and θ_D is evident in the deep coupling between trajectory morphology and equilibrium region stability.

Next, we will discuss how the hysteresis coefficient h and deadband threshold θ_D synergistically regulate phase trajectories and system stability under disturbance-free conditions. Adjusting the hysteresis coefficient to $h = 0.5$, while keeping the deadband threshold and acceleration amplitude constant, produced the phase trajectory diagram shown in Figure 6.

The hysteresis coefficient controls the characteristics of trajectory transitions by altering the hysteresis width. As h increases, the hysteresis boundary approaches the origin, thereby widening the hysteresis width. This broadens the buffer zone through which the trajectory transitions from the saturation region to the dead zone. This suppresses high-frequency switching and shortens the oscillation period. However, as the trajectory approaches the dead zone boundary, its amplitude increases. Conversely, decreasing h narrows the transition interval, causing frequent controller switching. This reduces the amplitude of the trajectory, but intensifies high-frequency oscillations and prolongs the period. With

the hysteresis coefficient and acceleration amplitude held constant, setting the deadband threshold θ_D to 1.5 yields the phase trajectory diagram shown in Figure 7.

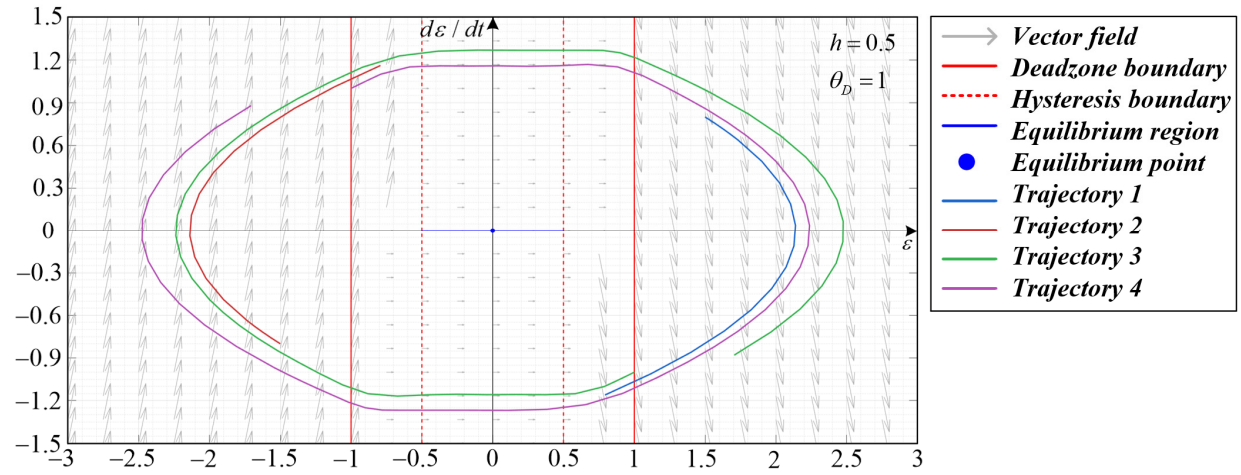


Figure 6. Phase trajectory diagram of an undisturbed system after adjustment of the hysteresis coefficient.

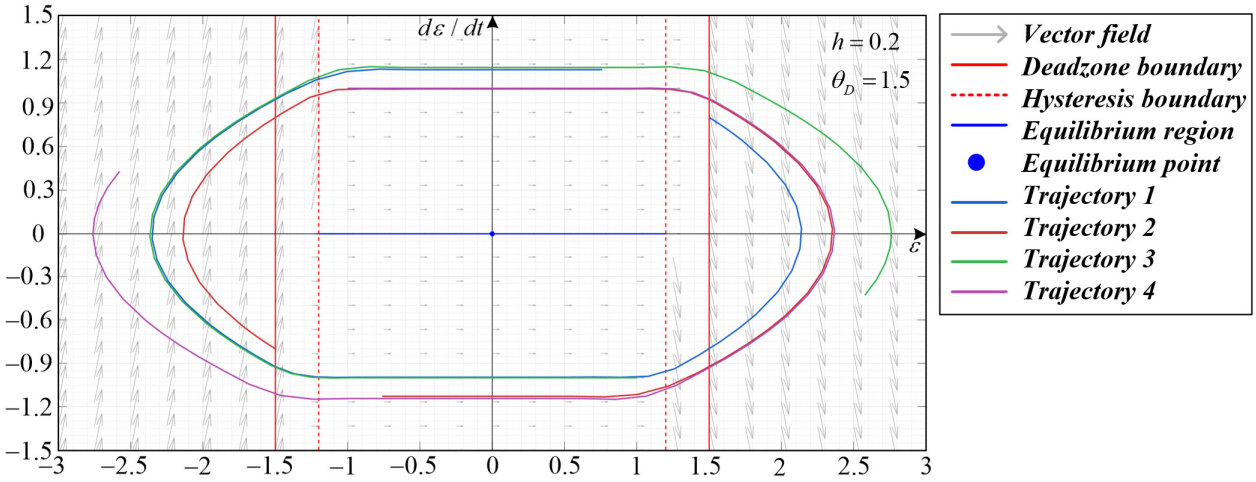


Figure 7. Phase trajectory diagram of the disturbance-free system after adjusting the deadband threshold.

The deadband threshold θ_D directly determines the extent of the deadband and hysteresis regions. As θ_D increases, the boundaries of these regions expand simultaneously, resulting in the equilibrium and buffer zones broadening. At the same time, the maximum oscillation amplitude increases due to constraints imposed by the deadband boundary, and the time required for convergence from the initial state to the equilibrium region increases accordingly.

In an undisturbed scenario, the system's stability depends primarily on the equilibrium region's asymptotic stability. From a Lyapunov stability perspective, increasing h broadens the equilibrium region while slowing the convergence rate. Concurrently, a wide hysteresis loop exerts a stronger damping effect on minor error fluctuations within the equilibrium region, thereby enhancing the margin of asymptotic stability. Conversely, decreasing h narrows the equilibrium region, steepens the transition gradient from the saturation zone to the hysteresis zone and accelerates convergence to the equilibrium region. However, narrow hysteresis bands can easily induce boundary oscillations, causing minor oscillations within the equilibrium region and reducing local stability margins. Increasing θ_D broadens

the equilibrium region, enhancing the system's tolerance to initial errors and expanding the attractor domain. However, the control inertia caused by the wide dead zone prolongs convergence time and weakens local asymptotic stability. Decreasing θ_D, on the other hand, shrinks the attractor domain but shortens the convergence path, thereby increasing the local stability margin.

3.4. Analysis of System Disturbance Presence

The subsequent discourse herein encompasses a detailed examination of two distinct scenarios, each characterised by the occurrence of disturbances. Initially, the case of $a_d \ll a_c$ is analysed, with $a_d > 0$ specified. The dynamic equation of the system under these conditions is as follows:

$$\ddot{\varepsilon} = -(a_c \cdot u_c + a_d) \tag{23}$$

For the condition $\varepsilon \geq \theta_D$, or $\varepsilon > (1-h)\theta_D$ (with $\dot{\varepsilon} < 0$), the system operates in the positive saturation region of the phase plane (where $u_c = 1$), and the corresponding dynamic equation is

$$\ddot{\varepsilon} = -(a_c + a_d) \tag{24}$$

Compared with the disturbance-free case, the phase trajectory moves clockwise with a slope of larger magnitude, leading to a faster rate of both increase and decrease in the error. For the condition $\varepsilon \leq -\theta_D$, or $\varepsilon < -(1-h)\theta_D$ (with $\dot{\varepsilon} > 0$), the system is located in the negative saturation region of the phase plane (where $u_c = -1$), and the dynamic equation is

$$\ddot{\varepsilon} = a_c - a_d \tag{25}$$

In this case, the phase trajectory moves clockwise with a slope of smaller magnitude, resulting in a slower rate of error variation (both increase and decrease). For the condition $-(1-h)\theta_D \leq \varepsilon < \theta_D$ (with $\dot{\varepsilon} > 0$), or $-\theta_D < \varepsilon \leq (1-h)\theta_D$ (with $\dot{\varepsilon} < 0$), the system lies in the dead zone of the phase plane (where $u_c = 0$), and the dynamic equation is

$$\ddot{\varepsilon} = a_d \tag{26}$$

The dead zone threshold is set to $\theta_D = 1$, the hysteresis coefficient to $h = 0.2$, the magnitude of the control acceleration to $a_c = 0.5$, and the disturbance acceleration to $a_d = 0.1$. The phase trajectory diagram of the system (under the presence of disturbance) is presented in Figure 8.

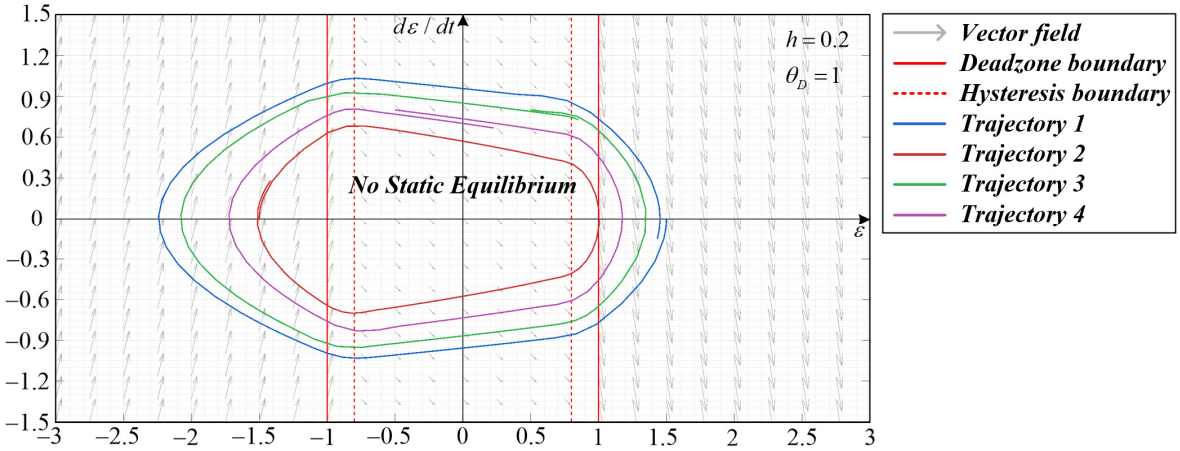


Figure 8. Phase trajectory diagram of the system under disturbance.

From Figure 8, it can be observed that when $a_d \ll a_c$, the phase trajectory still maintains limit cycle stability and exhibits no tendency to converge to a fixed point. Inside the dead zone, the disturbance induces a unidirectional variation in the error: the error continuously decreases until the negative saturation region is triggered, then rebounds to generate a limited deviation, ultimately forming a closed trajectory (i.e., a limit cycle). This characteristic reflects the robustness of the controller against weak disturbances: as long as the disturbance intensity does not exceed the control capability, the system error remains bounded, and the oscillation range can be optimised by adjusting the dead zone size θ_D and hysteresis width h.

Similarly, the co-regulation of the dead zone threshold θ_D and hysteresis coefficient h (on the phase trajectory and system stability) under the disturbance condition $a_d \ll a_c$ is discussed. By adjusting the hysteresis coefficient to $h = 0.5$ (while keeping the dead zone threshold and acceleration magnitude unchanged), the corresponding phase trajectory diagram is presented in Figure 9.

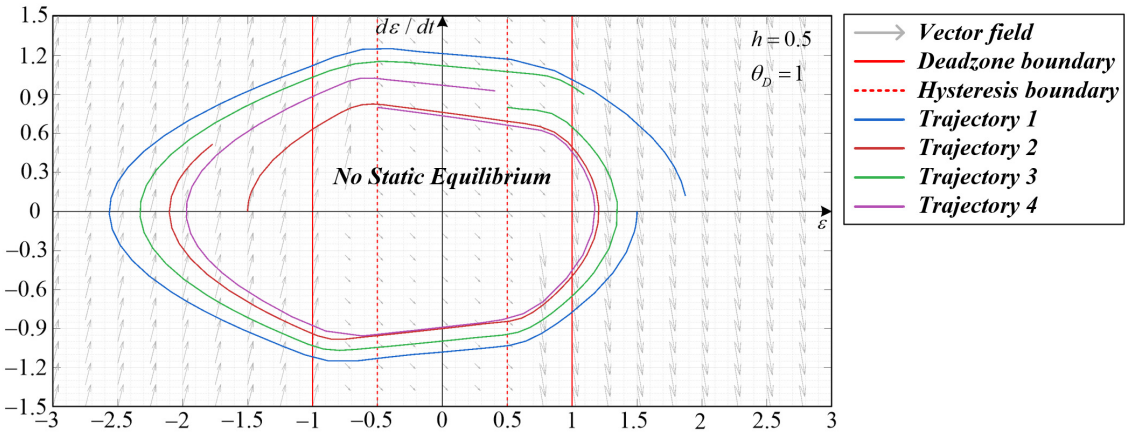


Figure 9. Phase trajectory diagram of the perturbed existence system after adjustment of the hysteresis coefficient.

It has been demonstrated that, in response to an increase in h, the buffer region of the dead zone–hysteresis controller undergoes an expansion in accordance with its switching logic. Specifically, when the trajectory moves from the dead zone boundary towards the origin, it must pass through a wider hysteresis region in order to exit saturation control. This leads to an extended movement time of the trajectory in the saturation region, accompanied by greater accumulation of control energy. The phase trajectory is characterised by the following manifestations: An augmentation in the limit cycle amplitude A reduction in the oscillation period A transition in loop morphology from "compact" to "expansive".

Concomitant with the maintenance of the hysteresis coefficient and acceleration magnitude, the dead zone threshold, denoted by the symbol θ_D, is adjusted to 1.5, and the corresponding phase trajectory diagram is presented in Figure 10.

As the θ_D increases, the boundaries of the dead zone expand, thereby enlarging the trajectory's operational space within this region. In the context of weak perturbations, the trajectory undergoes a transition from the saturation zone to the dead zone, resulting in an expansion of the dead zone area. This, in turn, leads to an augmentation of the uncontrolled drift time during periods of disturbance influence. This phenomenon leads to an augmentation in the oscillation range for each cycle. The phase trajectory results manifest as follows: a significant increase in the amplitude of the limit cycle, an elongation of the oscillation period, and a more gradual slope of the trajectory within the dead zone. Moreover, the expanded dead zone leads to a decline in the proportion of trajectory movement near the origin, consequently resulting in a flatter limit cycle shape.

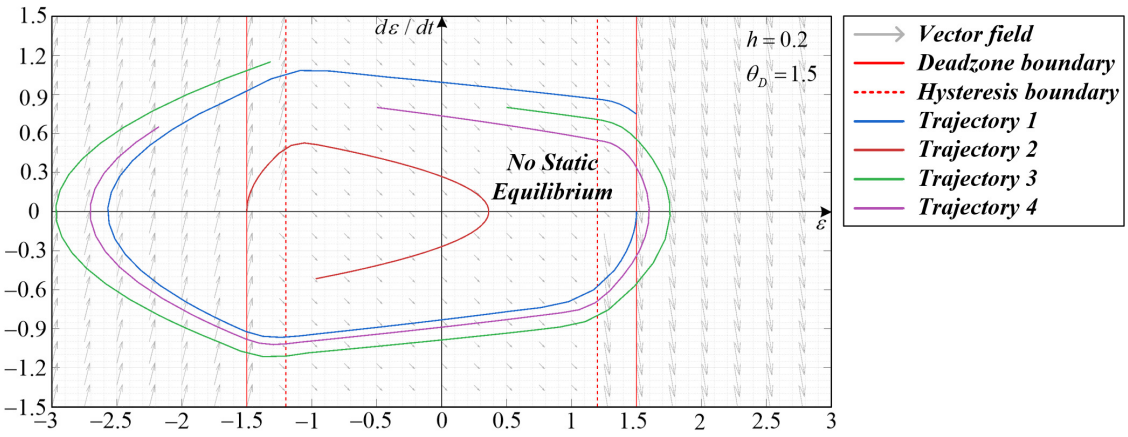


Figure 10. Phase trajectory diagram of the disturbance-prone system following adjustment of the deadband threshold.

The assessment of stability under weak perturbations is chiefly determined by the stability of the limit cycle trajectory. As the parameter h increases, the buffering effect of the wide hysteresis loop against disturbance energy strengthens. The application of transient micro-disturbances results in a wide hysteresis loop, which allows trajectory adjustments across a broader range. This prevents energy accumulation from frequent switching and enables gradual absorption of disturbance effects. It has been demonstrated that, as the limit cycle's tolerance to disturbances improves, the trajectory stability margin diminishes. Conversely, when h decreases, the narrow hysteresis loop renders the controller more sensitive to trajectory deviations; even minor disturbances trigger control actions, rapidly correcting trajectory shifts. The outcomes pertaining to stability can be summarised as follows: an augmentation in the trajectory stability margin is observable, whilst concomitantly, the disturbance filtering capability is diminished. In the context of narrow hysteresis loops, frequent controller switching enables the accumulation of energy in high-frequency disturbances through the action of switching. This process has the potential to induce minor oscillations in the limit cycle. The deadband threshold exerts a significant influence on stability, accomplished by modulating the disturbance filtering capability and control response speed. This modulating process can be conceptualised as a trade-off between filtering minor disturbances and delaying responses to major disturbances. It has been demonstrated that, as the θ_{D} increases, a considerable deadband is employed, thereby filtering out minor disturbances. However, it has also been observed that this deadband amplifies significant disturbances that occur in the vicinity of the deadband boundary, a phenomenon that can be attributed to the delayed intervention of control mechanisms. The outcomes of stability are manifest in two ways. Firstly, there is an enhancement of robustness against minor disturbances. However, secondly, there is a reduction in resilience to major disturbances. Furthermore, an extensive deadband serves to diminish the limit cycle's resilience to drift, thereby rendering the loop susceptible to gradual displacement in the presence of sustained disturbances. When θ_{D} decreases, a narrow deadband enables more timely controller responses to disturbances but fails to filter out minute disturbances, leading to energy accumulation from high-frequency switching. The outcomes of stability are manifest in two distinct forms. Firstly, there is an enhancement of robustness against large disturbances; secondly, there is a reduction in robustness against small disturbances. Concurrently, under narrow deadband constraints, the stability of the centre position within the limit cycle is enhanced, as control actions can expeditiously counteract the cumulative effects of disturbances.

Finally, the case where $a_c \ll a_d$ is discussed. When $a_c \ll a_d$, the disturbance term dominates the system: the error will increase or decrease unbounded, and the phase

trajectory exhibits a divergent state. By setting $a_d = 1$, the corresponding phase plane diagram is presented in Figure 11.

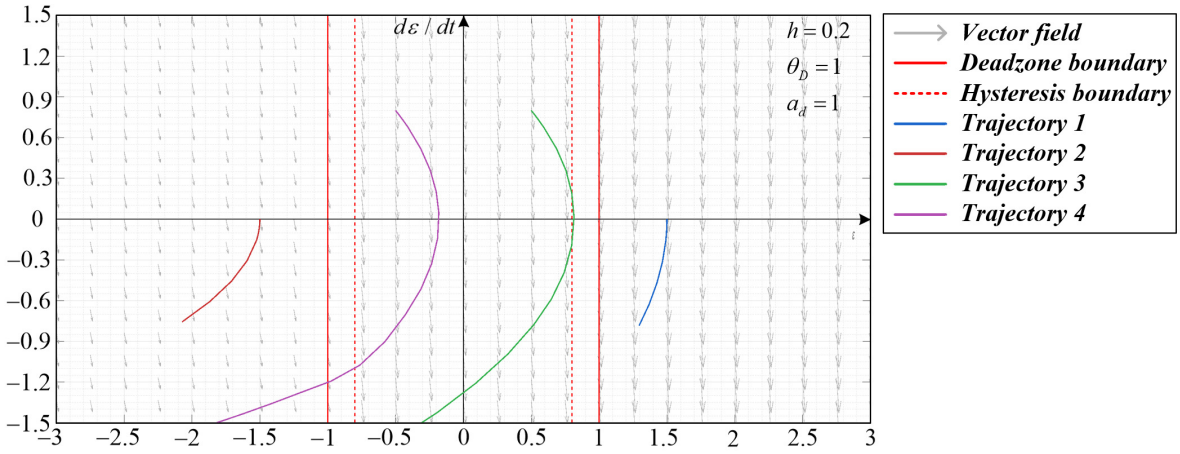


Figure 11. Phase trajectory diagram of a system with excessive disturbance.

In the presence of substantial disturbance conditions, the deadband–hysteresis controller's capacity to counteract disturbances is inadequate. This results in the system transitioning from bounded oscillations to unbounded divergence, accompanied by an infinite increase in attitude error until ultimately leading to control failure. This deficiency is attributable to the controller's fixed threshold in conjunction with its open-loop control architecture. Specifically, the thresholds for deadband and hysteresis are pre-set constants incapable of dynamic adjustment according to disturbance intensity. Moreover, the controller produces a fixed acceleration output via switch logic, exhibiting an absence of both disturbance perception and compensation capabilities.

In summary, the deadband–hysteresis nonlinear controller is a nonlinear system incorporating deadband relay characteristics, capable of suppressing high-frequency oscillations while achieving rapid response. However, the accuracy and disturbance rejection of the system are constrained by fixed parameters and switching logic, and thus, require improvement. The hysteresis coefficient h is a dimensionless parameter, typically ranging from 0 to 1, which is utilised to define the width of the hysteresis loop. Its function is to introduce a hysteresis interval, $h\theta_{\mathrm{D}}$, in the direction of error change, thereby reducing frequent controller switching near the transition point. This directly influences system stability and response speed. For instance, when the error increases to a certain threshold, the controller does not switch immediately; instead, it requires the error to exceed a certain percentage of that threshold before triggering the switch. The controller utilises distinct switching thresholds for increasing and decreasing errors, thereby forming an asymmetric switching logic known as the hysteresis effect. To illustrate this, consider an error that rises from low to high. In this scenario, it is necessary to reach a higher threshold, θ_{D}, in order to trigger controller action. Conversely, an error that falls from high to low necessitates reaching a lower threshold, $(1-h)\theta_{\mathrm{D}}$, to cease action. The dual-threshold design is intended to prevent frequent control state switching due to minor disturbances near the setpoint. This is believed to result in the suppression of high-frequency oscillations and enhancement of robustness. The deadband configuration of the controller is engineered to attain static equilibrium within the specified range through the deliberate suppression of control inputs, thereby establishing $\dot{\varepsilon} = 0$. This mechanism serves to circumvent superfluous control actions, thereby enhancing system stability and optimising energy efficiency.

An analysis of the deadband–hysteresis relay controller under multiple operating conditions via the phase plane method reveals the following: Despite the fact that this con-

troller has the capacity to circumvent minor errors through redundant control mechanisms, such as dead zones, and to suppress high-frequency jitter via hysteresis, thereby fulfilling the fundamental requirements for the attitude control of spacecraft simulation components, it is evident that the controller exhibits four core limitations. Firstly, steady-state accuracy is constrained due to the presence of dead zones, which prevent error convergence to zero. Consequently, maintenance is only possible within a preset range, rendering the system unsuitable for high-precision Earth-pointing tasks. Secondly, the system demonstrates a weak disturbance rejection capability. In the presence of weak disturbances, the system exhibits a propensity for limit-cycle oscillations. Conversely, under strong disturbances, the control torque is unable to counteract the disturbance, resulting in the divergence of the phase trajectory. Thirdly, the parameter adaptability of the system is suboptimal. The hysteresis coefficient and deadband threshold are immutable values, incapable of dynamic adjustment in accordance with real-time error and disturbance intensity. This inherent limitation gives rise to the paradoxical phenomenon of 'excessive deadband under weak disturbances and insufficient deadband under strong disturbances'. Fourthly, the system exhibits a deficiency in dynamic compensation, with a reliance on error and error derivative-based decision-making. This approach does not take into account the inertial characteristics of the analogue components or unmodelled dynamics. Consequently, it is unable to proactively estimate and counteract total disturbances. These issues directly constrain improvements in attitude control performance, necessitating the introduction of a more robust control framework for enhancement.

4. Design and Analysis of a Dead-Time–Hysteresis Relay Controller Based on Self-Disturbance Suppression Control

In addressing the inherent limitations of deadband–hysteresis relay controllers in steady-state accuracy, disturbance rejection capability, and parameter adaptability, as revealed in Section 3, this section introduces the ADRC theory and proposes an improved controller design that simultaneously incorporates "nonlinear switching characteristics" and "auto disturbance rejection capability." The core design approach is founded upon the following principles: The transient characteristics of the reference signal are optimised through NTD to resolve overshoot in step command responses. The limitations of traditional controllers' "passive disturbance rejection" are overcome by employing NESO for real-time estimation and compensation of total system disturbances. The original deadband–hysteresis controller is embedded within the nonlinear feedback loop of ADRC, and dynamic parameter adjustment logic is designed to achieve adaptive tuning of hysteresis width and deadband threshold. Furthermore, the section rigorously verifies the theoretical reliability of the improved controller through local stability analysis (Routh-Hurwitz criterion) and global stability analysis (Lyapunov function method), providing a solid theoretical foundation for subsequent simulation validation.

4.1. Design of NTD

The function of the tracking differentiator is to provide two signals: one is the target point transition signal, and the other is the differential signal of the target point transition signal. The transition signal can be considered as facilitating the system's incremental approach to the target point, thereby preventing sudden changes and overshoot. Therefore, the transition signal functions as an inertia element, thereby facilitating the gradual generation of a curve that approaches the target point, while simultaneously ensuring that overshooting is prevented.

The tracking differentiator provides two signals: one representing the transition signal of the target point and the other representing the differential of this transition. The transition signal can be understood as the gradual approach to the target point, without any abrupt

changes or overshoot. In other words, the transition signal can be interpreted as an inertial component that avoids overshoot and generates a curve towards the target point gradually.

The NTD first establishes a second-order integrated series system, the differential equation of which is

$$\begin{cases} \dot{x}_1 = x_2 \\ \dot{x}_2 = u \end{cases} \tag{27}$$

Optimal control of a system requires deriving a control strategy based on the system equations, initial conditions, terminal conditions, constraints, and cost function, such that the value of the cost function is minimised whilst satisfying the conditions and constraints.

The second-order integral series system equations may also be expressed as

$$\dot{x} = \begin{bmatrix} 0 & 1 \\ 0 & 0 \end{bmatrix} x + \begin{bmatrix} 1 \\ 0 \end{bmatrix} u \tag{28}$$

The system's initial, boundary and constraint conditions are, respectively, as follows:

$$x(0) = \begin{bmatrix} x_1(0) \\ x_2(0) \end{bmatrix} + \begin{bmatrix} z_1 \\ z_2 \end{bmatrix}, \; x\left(t_f\right) = \begin{bmatrix} x_1\left(t_f\right) \\ x_2\left(t_f\right) \end{bmatrix} + \begin{bmatrix} 0 \\ 0 \end{bmatrix}, \; |u| \le r \tag{29}$$

Here, r denotes the rapid tracking factor: the greater r's value, the faster the system tracks the desired value. However, when r increases beyond a certain threshold, the approach speed does not change significantly. If the aim is for the system to reach the terminal condition at the fastest possible rate, the performance metric is denoted as

$$J = \int_{t_d}^{t_f} 1 dt \tag{30}$$

The Hamiltonian function can thus be obtained:

$$H(x(t), u(t), \lambda(t), t) = 1 + \lambda_1(t) x_2(t) + \lambda_2(t) u(t) \tag{31}$$

According to the classical variational approach, the conditions for optimising performance metrics are as follows:

$$\begin{cases} \frac{\partial H}{\partial \lambda} - \dot{x} = 0 \\ \frac{\partial H}{\partial x} + \dot{\lambda} = 0 \\ \frac{\partial H}{\partial u} = 0 \end{cases} \tag{32}$$

Further obtained is the following:

$$\begin{bmatrix} x_2 \\ u \end{bmatrix} - \begin{bmatrix} \dot{x}_1 \\ \dot{x}_2 \end{bmatrix} = 0, \begin{bmatrix} 0 \\ \lambda_1 \end{bmatrix} + \begin{bmatrix} \dot{\lambda}_1 \\ \dot{\lambda}_2 \end{bmatrix} = 0, \lambda_2 = 0 \tag{33}$$

At this point, a contradiction arises: since the Hamilton function is linear in u, the extremum must exist and lie on the boundary rather than at the point where the partial derivative is zero. According to the conjugate condition equation

$$\begin{bmatrix} 0 \\ \lambda_1 \end{bmatrix} + \begin{bmatrix} \dot{\lambda}_1 \\ \dot{\lambda}_2 \end{bmatrix} = 0 \tag{34}$$

We can obtain

$$\begin{cases} \lambda_1^*(t) = C_1 \\ \lambda_2^*(t) = -C_1 t + C_2 \end{cases} \tag{35}$$

From the Minimum Principle, it follows that when the Hamiltonian $H = 1 + \lambda_1(t)x_2(t) + \lambda_2(t)u(t)$ attains its minimum, the term $\lambda_2(t)u(t)$ also reaches its minimum. Given the constraint $|u| \leq r$, the optimal control $u^*(t)$ is determined as $u^*(t) = -rsign(\lambda_2^*(t))$. When $\lambda_2^*(t) = -C_1t + C_2 > 0$, we obtain $u^*(t) = -r$. Furthermore, based on the initial conditions, we can derive that

$$\begin{cases} x_2(t) = z_2 - rt \\ x_1(t) = z_1 + z_2t - \frac{1}{2}rt^2 \end{cases} \tag{36}$$

Eliminating t yields

$$x_1(t) = -\frac{1}{2r}{x_2}^2(t) + z_1 + \frac{1}{2r}{z_2}^2 \tag{37}$$

Similarly, when $\lambda_2^*(t) = -C_1t + C_2 < 0$,

$$x_1(t) = \frac{1}{2r}{x_2}^2(t) + z_1 - \frac{1}{2r}{z_2}^2 \tag{38}$$

Depending on the initial value, the optimal control alternates between r and $-r$. Considering the curve passing through the origin, we have

$$\begin{cases} u = -r, x_1(t) = -\frac{1}{2r}{x_2}^2(t), x_2(t) \geq 0 \\ u = r, x_1(t) = \frac{1}{2r}{x_2}^2(t), x_2(t) \leq 0 \end{cases} \tag{39}$$

The switch function can be expressed as

$$\begin{cases} x_1(t) = -\frac{x_2(t)|x_2(t)|}{2r} \\ u = -rsign\left(x_1 + \frac{x_2|x_2|}{2r}\right) \end{cases} \tag{40}$$

Therefore, the NTD is obtained by setting the control rate of the controlled variable u as the composite function of rapid optimal control and treating x_1 as the target transition signal and x_2 as the differential signal of the target transition signal:

$$\begin{cases} \dot{x}_1 = x_2 \\ \dot{x}_2 = -rsign\left(x_1 - \varepsilon + \frac{x_2|x_2|}{2r}\right) \end{cases} \tag{41}$$

Here, x_1 denotes the current error and ε represents the target input error. The contents within the function brackets can be seen as having two parts: the 'displacement' of the target error and the 'displacement' during the process of reducing the error velocity to zero. When the 'displacement' of the target error exceeds the 'displacement' of the deceleration process—meaning that decelerating to zero fails to achieve the target error—the error decelerates with acceleration $u = -r$. Conversely, the error accelerates with acceleration $u = r$.

4.2. Design of Observers for Nonlinear Expanding States

The ESO, in a sense, constitutes a versatile and practical disturbance observer. The control block diagrams for the basic state observer and the ESO are illustrated in Figure 12. Compared to the pre-extension state, the ESO estimates the system's 'total disturbance' or 'unknown disturbance'. The core concept of the ESO is to expand the disturbance affecting the controlled output into new state variables, employing a special feedback mechanism to establish observability of the expanded states. The ESO does not rely on the specific mathematical model generating the disturbance—namely, the function f describing the

object's transfer relationship—nor does it require direct measurement of its effect. It utilises only the input–output information of the original object.

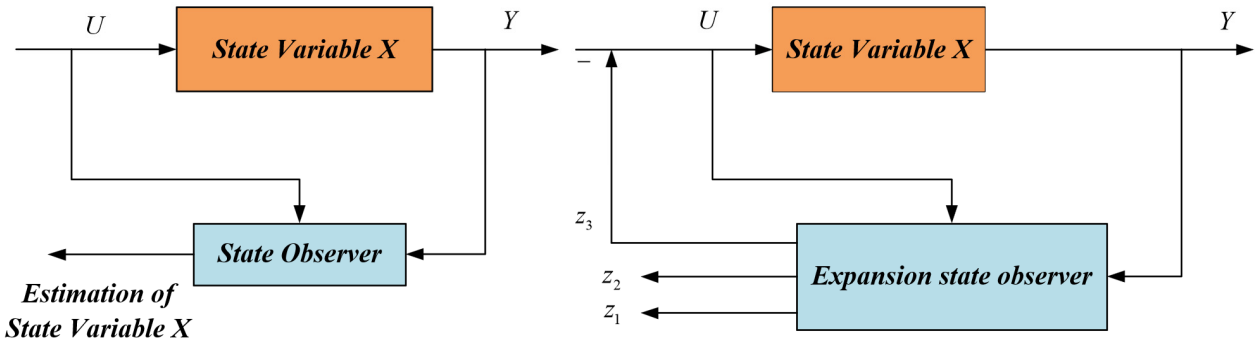


Figure 12. Basic state observer and ESO.

For a typical system,

$$\begin{cases} \dot{\mathbf{X}}=\mathbf{AX}+\mathbf{BU} \\ \mathbf{Y}=\mathbf{CX} \end{cases} \tag{42}$$

Let **X** be an n-dimensional state variable, **U** and **Y** be p-dimensional and q-dimensional vectors, respectively (typically $q < n, p < n$). By taking the output vector **Y** and input vector **U** of the plant as inputs, the following new system can be constructed:

$$\dot{\mathbf{Z}} = \mathbf{AZ} - \mathbf{L}(\mathbf{CZ} - \mathbf{Y}) + \mathbf{BU}=(\mathbf{A} - \mathbf{LC}) + \mathbf{LY} + \mathbf{BU} \tag{43}$$

In this equation, **Z** denotes the estimated state vector; **L** is an appropriately selected matrix. This new system is designed using the output vector **Y** and input vector **U** of the plant. Let $e = \mathbf{Z} - \mathbf{X}$ represent the error between the state variables of the two systems. Subtracting the equations of the two systems yields the system of equations satisfied by the error variable e:

$$\dot{e} = (\mathbf{A} - \mathbf{LC})e \tag{44}$$

As long as the matrix **L** is chosen to render $(\mathbf{A} - \mathbf{LC})$ stable, e will converge to 0, and thus **Z** will approach **X**. The state **Z** of the newly designed system can approximately estimate all state variables **X** of the original system. When the above conditions are satisfied, the newly constructed system is referred to as the state observer of the original system. This state observer can also be rewritten as

$$\begin{cases} e = \mathbf{CZ} - \mathbf{Y} \\ \dot{\mathbf{Z}} = \mathbf{AZ} - \mathbf{L}e + \mathbf{BU} \end{cases} \tag{45}$$

Here, e is the output error of the system. Thus, the state observer is a new system constructed by modifying the original system via the feedback of the output error.

For the dead zone–hysteresis relay controller, if the disturbance term a_d is no longer a constant but a nonlinear function $f(\varepsilon, \dot{\varepsilon})$ of ε and $\dot{\varepsilon}$, the state variable is defined as

$$\mathbf{X} = \begin{bmatrix} x_1 \\ x_2 \end{bmatrix} = \begin{bmatrix} \varepsilon \\ \dot{\varepsilon} \end{bmatrix} \tag{46}$$

Then the following nonlinear system can be established:

$$\begin{cases} \dot{x}_1 = x_2 \\ \dot{x}_2 = f(x_1, x_2) + a_c u \\ y = x_1 \end{cases} \tag{47}$$

When the function $f(x_1, x_2)$ is not specifically determined a_c is known, the following state observer is constructed:

$$\begin{cases} e_1 = z_1 - y \\ \dot{z}_1 = z_2 - l_1 e_1 \\ \dot{z}_2 = -l_2 e_1 + a_c u \end{cases} \tag{48}$$

Here, the unknown function $f(x_1, x_2)$ is omitted; however, it still acts as a disturbance in the error system. To effectively suppress its influence, the following nonlinear feedback form is adopted based on the nonlinear feedback effect:

$$-\beta_{01} g_1(e), -\beta_{02} g_2(e) \tag{49}$$

Here, $g(e)$ is chosen as the fal function, which is a common nonlinear function used in ADRC. It exhibits distinct behaviours in different error regions. Small-error region: It shows linear characteristics, avoiding excessive sensitivity to minor disturbances and suppressing high-frequency noise. Large-error region: The error signal is amplified nonlinearly, accelerating the convergence speed of the observer. Additionally, the fal function has filtering properties. Compared with first-order filters, it achieves better filtering performance: the filtered signal can track the input signal rapidly without delay and the signal amplitude is barely affected. At this point, the nonlinear state observer is given by

$$\begin{cases} e_1 = z_1 - y \\ \dot{z}_1 = z_2 + \beta_{01} e_1 \\ \dot{z}_2 = \beta_{02} |e_1|^{\frac{1}{2}} sign(e_1) + a_c u \end{cases} \tag{50}$$

Next, the real-time disturbance $f(x_1(t), x_2(t))$ acting on this nonlinear open-loop system is expanded as a new state variable x_3, denoted as

$$x_3(t) = f(x_1(t), x_2(t)) \tag{51}$$

Let $\dot{x}_3(t) = \omega(t)$; then the system can be extended into a new nonlinear system:

$$\begin{cases} \dot{x}_1 = x_2 \\ \dot{x}_2 = x_3 + a_c u \\ \dot{x}_3 = \omega(t) \\ y = x_1 \end{cases} \tag{52}$$

The ESO for this expanded system is given by

$$\begin{cases} e_1 = z_1 - y \\ \dot{z}_1 = z_2 + \beta_{01} e_1 \\ \dot{z}_2 = z_3 + \beta_{02} |e_1|^{\frac{1}{2}} sign(e_1) + a_c u \\ \dot{z}_3 = \beta_{03} |e_1|^{\frac{1}{4}} sign(e_1) \end{cases} \tag{53}$$

In order to achieve the aforementioned objective, it is necessary to design the coefficients $\beta_{01}, \beta_{02}\beta_{03}$ of the ESO in such a manner that $e_1 \to 0$, thus facilitating state observation. Nonlinear functions have the capacity to either weaken or enhance the observer dynamics; therefore, adjustments should be made based on actual system responses. If the observer exhibits slow convergence and tracking lag, it is necessary to increase ω_0 to raise the gains $\beta_{01}, \beta_{02}, \beta_{03}$ of the system. If significant chattering occurs in the observed values, it is advisable to reduce ω_0 and lower the gains to suppress noise.

4.3. Improved Controller Design and Stability Analysis

The enhanced ADRC controller, as demonstrated in Figure 13, consists of four core modules arranged sequentially: the NTD, NESO, dynamic deadband module, adaptive hysteresis coefficient module, and deadband–hysteresis nonlinear feedback controller. The sequence of signal transitions is as follows: the command signal is initially input to the NTD, resulting in the generation of the target transition signal x_1 without overshoot and its derivative x_2. The NTD output x1 combines with the system attitude feedback z_1 to form the tracking error, which is then fed into the adaptive hysteresis coefficient module. Concurrently, the system output y and control input u are input to the NESO, which estimates and outputs the total disturbance z_3 and state estimates z_1, z_2 in real time. The tracking error is then entered into the adaptive hysteresis coefficient module, while the disturbance estimate z_3 is fed into the dynamic deadband module. The dynamic deadband module calculates and outputs the adaptive hysteresis width coefficient and deadband threshold in real time. In conclusion, the enhanced nonlinear feedback controller generates the ultimate output signal based on the error and its derivative, in conjunction with the compensated control law and dynamic parameters. This process ensures precise actuation of the actuator.

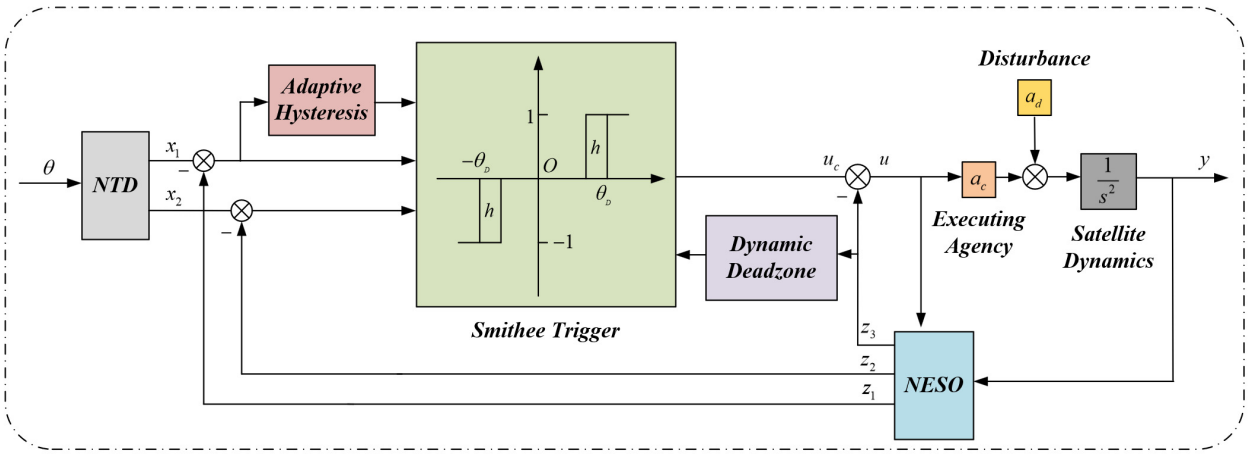


Figure 13. Block Diagram of an Improved Dead-Time–Hysteresis Relay Controller Based on ADRC.

The incorporation of the dead zone–hysteresis relay controller within the ADRC results in the non-linear control law of the new system becoming

$$u = \begin{cases} 1 - z_3 & \varepsilon \geq \theta_{\mathrm{D}} \\ 1 - z_3 & \varepsilon > (1 - h(t))\theta_{\mathrm{D}}, \dot{\varepsilon} < 0 \\ -z_3 & -(1 - h(t))\theta_{\mathrm{D}} \leq \varepsilon < \theta_{\mathrm{D}}, \dot{\varepsilon} > 0 \\ -z_3 & -\theta_{\mathrm{D}} < \varepsilon \leq (1 - h(t))\theta_{\mathrm{D}}, \dot{\varepsilon} < 0 \\ -1 - z_3 & \varepsilon \leq -\theta_{\mathrm{D}} \\ -1 - z_3 & \varepsilon < -(1 - h(t))\theta_{\mathrm{D}}, \dot{\varepsilon} > 0 \end{cases} \tag{54}$$

Herein, z_3 denotes the total system disturbance estimated by the NESO, θ_{D} is the dead zone threshold dynamically adjusted based on the disturbance estimate z_3, and $h(t)$ is the hysteresis width dynamically adjusted according to the real-time system error. The expressions for θ_{D} and $h(t)$ are given as

$$\begin{cases} \theta_{\mathrm{D}} = \theta_{\mathrm{D0}} + k_d |z_3| \\ h(t) = h_0 \cdot \left(1 - \frac{|e|}{e_{\max}}\right) \end{cases} \tag{55}$$

where k_d represents the sensitivity of the control dead zone to disturbance estimation; θ_{D0} is the initially set dead zone threshold; h_0 denotes the baseline hysteresis coefficient (it determines the maximum hysteresis width when the error is zero); $e_{\max}$ is the maximum allowable system error.

This paper builds upon an in-depth analysis and phase-plane method investigation of the dead-zone–hysteresis relay controller, the results of which identified the inherent limitations of the controller. These limitations are as follows: constrained steady-state accuracy, insufficient disturbance rejection capability, and potential limit-cycle oscillations or divergence under strong disturbances. In order to surmount these constraints, the present paper introduces a self-disturbance-rejection control framework for systematic enhancement, centred on the design and implementation of the NESO. The NESO offers a novel pathway to achieving high-precision control by real-time estimation and compensation of the total system disturbance. This section rigorously proves the stability of the NESO, thereby establishing a robust theoretical foundation for the entire ADRC enhancement scheme. This proof ensures the theoretical reliability of the controller and provides fundamental assurance for its effectiveness in practical engineering applications.

To establish the state-space model required for the NESO, we define the total disturbance as $\ddot{\theta} = a_c + a_d$ based on $f\left(\theta, \dot{\theta}\right) = a_d$. The system equation is then rewritten as

$$\ddot{\theta} = a_c + f\left(\theta, \dot{\theta}\right) \tag{56}$$

The following definition of state variables is proposed:

$$\begin{cases} x_1 = \theta \\ x_2 = \dot{\theta} \\ x_3 = f\left(\theta, \dot{\theta}\right) \end{cases} \tag{57}$$

The system state space equations are as follows:

$$\begin{cases} \dot{x}_1 = x_2 \\ \dot{x}_2 = x_3 + a_c \\ \dot{x}_3 = \omega(t) \end{cases} \tag{58}$$

Here, $\omega(t)$ denotes the bounded disturbance rate of change. In the NESO design section, the real-time disturbance $f(x_1(t), x_2(t))$ acting on this nonlinear open-loop system is expanded as a new state variable x_3. Accordingly, the state estimation equations of the NESO take the following nonlinear feedback form:

$$\begin{cases} \dot{z}_1 = z_2 + \beta_{01} g(e_1) \\ \dot{z}_2 = z_3 + \beta_{02} g(e_1) + a_c u \\ \dot{z}_3 = \beta_{03} g(e_1) \end{cases} \tag{59}$$

In these equations, $e_1 = z_1 - x_1$ is the observation error; $\beta_{01}, \beta_{02}, \beta_{03} < 0$ are the observer gain parameters. As mentioned earlier, the fal function is adopted as the nonlinear feedback $g(e)$:

$$fal(e, \alpha, \delta) = \begin{cases} |e|^{\alpha} \cdot sign(e), & |e| > \delta \\ e/\delta^{1-\alpha}, & |e| \le \delta \end{cases} \tag{60}$$

Here, α is an exponential parameter (satisfying $0 < \alpha < 1$) that controls the degree of nonlinearity; $\delta > 0$ is a threshold parameter that defines the width of the linear interval. An observation error vector is defined as

$$\begin{cases} e_1 = z_1 - x_1 \\ e_2 = z_2 - x_2 \\ e_3 = z_3 - x_3 \end{cases} \tag{61}$$

The error dynamics equation can be derived by subtracting the state derivatives of the observation system from those of the true system:

$$\begin{cases} \dot{e}_1 = \dot{z}_1 - \dot{x}_1 = e_2 + \beta_{01} fal(e_1, \alpha_1, \delta) \\ \dot{e}_2 = \dot{z}_2 - \dot{x}_2 = e_3 + \beta_{02} fal(e_1, \alpha_2, \delta) \\ \dot{e}_3 = \dot{z}_3 - \dot{x}_3 = \beta_{03} fal(e_1, \alpha_3, \delta) - \omega(t) \end{cases} \tag{62}$$

The Lyapunov stability analysis presented in this section is predicated on the assumption that the rate of change in the total disturbance is finite. This standard assumption aims to establish a clear theoretical benchmark for the convergence behaviour of the NESO. It is noteworthy that the fal nonlinear feedback function employed in this observer exhibits inherent structural robustness in practical applications. This robustness extends beyond the assumed constraints, accommodating disturbances with non-smooth or stochastic components. It is evident that the small-error linearisation and large-error saturation characteristics of fal facilitate this particular behaviour. The simulation validation in Section 5 below will confirm this engineering robustness.

The core objective of stability analysis is to demonstrate that as $t \to \infty$, the observation errors e_1, e_2, e_3 converge to zero or a bounded small range. First, local stability analysis is performed: this focuses on scenarios with small observation errors (i.e., $|e_1| \leq \delta$) where the fal function operates in the linear region. By linearizing the error dynamics equations and analysing the distribution of their eigenvalues, the asymptotic stability of the NESO in the small-error steady-state phase is verified.

When $|e_1| \leq \delta$, the fal function is linearized as

$$fal(e_1, \alpha, \delta) = \frac{e_1}{\delta^{1-\alpha}} = k e_1 \tag{63}$$

Substituting this into the error dynamics equations yields the linearized error system:

$$\dot{e} = Ae + B\omega(t) \tag{64}$$

where the system matrices are

$$A = \begin{bmatrix} \beta_{01} k & 1 & 0 \\ \beta_{02} k & 0 & 1 \\ \beta_{03} k & 0 & 0 \end{bmatrix}, B = \begin{bmatrix} 0 \\ 0 \\ -1 \end{bmatrix} \tag{65}$$

The characteristic equation of the system matrix A is then

$$\det(\lambda I - A) = \lambda^3 - \beta_{01} k \lambda^2 - \beta_{02} k \lambda - \beta_{03} k = 0 \tag{66}$$

The Routh-Hurwitz criterion is applied here. The necessary and sufficient conditions for the system to be asymptotically stable are

$$\begin{cases} -\beta_{01}k > 0 \\ -\beta_{03}k > 0 \\ \beta_{01}k \cdot \beta_{02}k > -\beta_{03}k \end{cases} \tag{67}$$

Since $k = \frac{1}{\delta^{1-\alpha}}$ and $\beta_{01}, \beta_{02}, \beta_{03} < 0$, only the following condition needs to be satisfied:

$$\beta_{01} \cdot \beta_{02} > -\beta_{03}\delta^{1-\alpha} \tag{68}$$

It is evident that at this juncture, the system stability criterion is satisfied, and NESO is locally asymptotically stable.

Next, global stability analysis is performed. This analysis targets scenarios with arbitrary initial observation errors (covering the region where $|e_1| > \delta$). By constructing a Lyapunov function, the globally uniformly ultimately bounded property of the error system is proven.

A quadratic Lyapunov function is selected as follows:

$$V(e_1, e_2, e_3) = \frac{1}{2}{e_1}^2 + \frac{1}{2}{e_2}^2 + \frac{1}{2}{e_3}^2 \tag{69}$$

Obviously, $V > 0$ holds for all $(e_1, e_2, e_3) \neq (0, 0, 0)$, and $V(0, 0, 0) = 0$, which satisfies positive definiteness.

The time derivative of V is calculated as

$$\dot{V} = e_1\dot{e}_1 + e_2\dot{e}_2 + e_3\dot{e}_3 \tag{70}$$

Substituting the error dynamics equations into the above expression yields

$$\begin{aligned} \dot{V} &= e_1(e_2 + \beta_{01}fal(e_1, \alpha_1, \delta)) + e_2(e_3 + \beta_{02}fal(e_1, \alpha_2, \delta)) + e_3(\beta_{03}fal(e_1, \alpha_3, \delta) - \omega(t)) \\ &= e_1e_2 + e_2e_3 + e_1\beta_{01}fal(e_1, \alpha_1, \delta) + e_2\beta_{02}fal(e_1, \alpha_2, \delta) + e_3\beta_{03}fal(e_1, \alpha_3, \delta) - e_3\omega(t) \end{aligned} \tag{71}$$

Since the fal function exhibits positive definite dissipativity, for any $e \in \mathbb{R}$, the following holds

$$e \cdot fal(e, \alpha, \delta) \geq \min(1, \delta^{\alpha})|e|^{\alpha+1} > 0, (e \neq 0) \tag{72}$$

Combining the boundedness of the disturbance ($|\omega(t)| \leq F_{\max}$, where $F_{\max}$ denotes the upper bound of the maximum absolute value of the disturbance rate of change), each term is estimated. For the cross terms,

$$e_1e_2 + e_2e_3 \leq \frac{1}{2}{e_1}^2 + {e_2}^2 + \frac{1}{2}{e_3}^2 \tag{73}$$

For the dissipative terms, let $k_0 = \min(1, \delta^{\alpha_1}, \delta^{\alpha_2}, \delta^{\alpha_3})$; then,

$$\begin{aligned} \beta_{01}e_1fal(e_1, \alpha_1, \delta) &\geq \beta_{01}k_0|e_1|^{\alpha_1+1} \\ \beta_{02}e_2fal(e_1, \alpha_2, \delta) &\geq \beta_{02}k_0|e_1|^{\alpha_2+1} \\ \beta_{03}e_3fal(e_1, \alpha_3, \delta) &\geq \beta_{03}k_0|e_1|^{\alpha_3+1} \end{aligned} \tag{74}$$

Similarly, for the disturbance term,

$$|e_3\omega(t)| \leq \frac{1}{2}{e_3}^2 + \frac{1}{2}F_{\max}^2 \tag{75}$$

Substituting the above estimations into $\dot{V}$ and rearranging yields

$$\dot{V} \leq \frac{1}{2}{e_1}^2 + {e_2}^2 + \beta_{01}k_0|e_1|^{\alpha_1+1} + \beta_{02}k_0|e_1|^{\alpha_2+1} + \beta_{03}k_0|e_1|^{\alpha_3+1} - \frac{1}{2}F_{\max}^2 \tag{76}$$

When $e_1 > \Delta$ (where Δ is a bounded threshold satisfying $\beta_{01}k_0\Delta^{\alpha_1+1} = \frac{1}{2}\Delta^2$), the following holds

$$-\beta_{01}k_0\Delta^{\alpha_1+1} < -\frac{1}{2}{e_1}^2 \tag{77}$$

Similarly, the same treatment is applied to the terms involving β_{02} and β_{03}. At this point,

$$\dot{V} \leq -\frac{1}{2}\left({e_1}^2 + {e_2}^2 + {e_3}^2\right) - \frac{1}{2}F_{\max}^2 \tag{78}$$

This indicates that $\dot{V}$ is negative definite. According to the globally uniformly ultimately bounded theorem, there exists a constant $B > 0$ such that as $t \to \infty$, the observation errors e_1, e_2, e_3 converge to a bounded set. In other words, the NESO possesses globally uniformly ultimately bounded stability.

4.4. Convergence Analysis of Estimation Errors in Disturbance Models

The convergence of disturbance estimation errors is indicative of the NESO's robustness.

The third equation of error dynamics is as follows:

$$\dot{e}_3 = \beta_{03}fal(e_1, \alpha_3, \delta) - \omega(t) \tag{79}$$

When the system enters the steady state $e_1 \to \infty$, $fal(e_1, \alpha_3, \delta) \approx ke_1 \to 0$, so $\dot{e}_3 \approx -\omega(t)$. Integrating this yields

$$e_3(t) \approx e_3(0) - \int_0^t \omega(\tau)d\tau \tag{80}$$

Since $\omega(t)$ is bounded, the rate of change of $e_3(t)$ is finite. Combined with the conclusions of Lyapunov analysis, the convergence speed of the disturbance estimation error is positively correlated with the observer gain.

When the system is in the steady state, e_1 converges to a minimal range, and $\dot{e}_3 \approx \beta_{03}k(e_1, \alpha_3, \delta) - \omega(t)$ at this point. Since the steady-state value of e_1 is negligible, the steady-state value of the disturbance estimation error is mainly determined by $\omega(t)$ and β_{03}:

$$e_3(\infty) \approx \frac{|\omega(t)|}{\beta_{03}k} \tag{81}$$

The order of magnitude of this value is 1×10^{-4}, which is much smaller than the control acceleration, indicating that the impact of the disturbance estimation error on control performance is negligible.

This section thus represents the culmination of the design and theoretical validation of an enhanced dead-zone–hysteresis controller based on ADRC. The core achievements are reflected in three aspects: firstly, the generation of an overshoot-free, fast-response target transition signal via an NTD resolves the original controller's overshoot issue for step commands; secondly, real-time disturbance estimation and active compensation are achieved by expanding the total disturbance into new state variables via NESO. The local asymptotic stability and global uniform boundedness of the system have been rigorously proven. Thirdly, a dynamic parameter adjustment logic based on error and disturbance estimates has been devised, enabling adaptive matching of hysteresis width and deadband

threshold to operating conditions. This fundamental innovation effectively addresses the inherent limitations of the original controller, which were a consequence of the fixed parameters. Convergence analysis of disturbance estimation errors demonstrates the NESO's high disturbance estimation accuracy, with negligible impact on control performance.

5. Test Results

In Section 4, the theoretical design of an enhanced controller founded upon ADRC has been concluded. This design has been demonstrated to resolve the original controller's deficiencies, namely its substandard steady-state accuracy and inadequate disturbance rejection. Nevertheless, the validation of its effectiveness and engineering practicality remains to be substantiated through simulation under actual operating conditions. This section employs real data from ground-based full-physical spacecraft docking performance experiments as the comparative benchmark. A triad of core operational simulation scenarios has been devised with the objective of comprehensively validating the engineering adaptability and performance advantages of the enhanced ADRC-based deadband–hysteresis controller. The simulation environments meticulously replicate the critical operational characteristics of the ground experiments.

In order to ascertain the fundamental operating condition, the attitude setting of the spacecraft mock-up in the experiment was compared with the actual attitude data from the experiment. This finding serves to validate the efficacy of the enhanced algorithm in the context of steady-state error control and low-redundancy control actions, thereby ensuring that the spacecraft model meets the 'high-precision, low-loss' requirements during routine operations.

In order to account for the dynamic conditions that prevail during the separation experiments, where the connector maintains a stable attitude prior to disengagement, a comparison was made between the simulation outcomes and the actual experimental attitude data. This finding serves to substantiate the algorithm's efficacy in mitigating transient disturbances and its expeditious attitude recovery performance, thereby underscoring its capacity to adeptly manage sudden disturbances during separation.

In addressing the critical operational scenario requiring rapid and precise establishment of initial roll and pitch conditions prior to docking, the improved algorithm's performance in rapid attitude adjustment and overshoot-free response was validated through comparison of simulation results with actual experimental data. This ensures that the craft meets the docking mission's requirements for 'rapid convergence and high precision' in initial attitude.

The enhanced algorithm's performance in steady-state accuracy, disturbance rejection capability, and rapid response is evaluated by quantifying the consistency between simulation outcomes and ground-test data. This provides a foundation of empirical evidence upon which to base the practical engineering deployment of the system.

5.1. Parameter Selection Specifications and Sensitivity Analysis

The parameter design of this controller adheres to the principle of combining theoretical guidance with engineering optimisation, with the following specifications:

(1) Initial static parameters: The deadband threshold, designated as θ_{D0}, has been determined to be 0.001, and the hysteresis coefficient, denoted as h_0, has been established as 0.1. These parameters are deduced through phase plane analysis, a method that ensures the system's convergence to the equilibrium region in the absence of external disturbances. The fast-tracking factor r is optimised through NTD transition process planning, balancing response speed and overshoot suppression.

(2) Dynamic adjustment law design: The dynamic adjustment of parameters θ_D and h incorporates disturbance estimation sensitivity k_d and error normalisation factor $e_{\max}$, forming Equation (55). In this configuration, k_d guarantees that for each unit increase in $|z_3|$, θ_D expands by 0.01°, thereby preventing high-frequency actuator switching. Furthermore, $e_{\max}$ imposes limitations on the adaptive range of the lag coefficient, thereby enhancing steady-state accuracy.

(3) NESO Gain Stability Constraints: It is imperative that the β_{01}, β_{02}, β_{03} values satisfy the Routh-Hurwitz conditions to ensure that the observation error remains globally bounded.

(4) Parameter tuning procedure: Initial values are established in accordance with theoretical constraints. Subsequently, a series of parameter sweep simulations are conducted under three typical operating conditions. The optimisation targets encompass a steady-state error of less than ±0.01°, a convergence time of less than 3 s, and the absence of overshoot. The final values align with the data obtained from the ground tests.

5.2. Standard Posture Configuration

The system parameters for conventional attitude setting are shown in Table 2.

Table 2. System parameters for conventional attitude setting.

System Parameters	Data	System Parameters	Data
h_0	0.1	β_{01}	−20
$e_{\max}$	0.01	β_{02}	−300
θ_{D0}	0.001	β_{03}	−20
k_d	0.01	a_c	5
r	5		

The simulation results corresponding to this conventional attitude setting are presented in Figures 14–16.

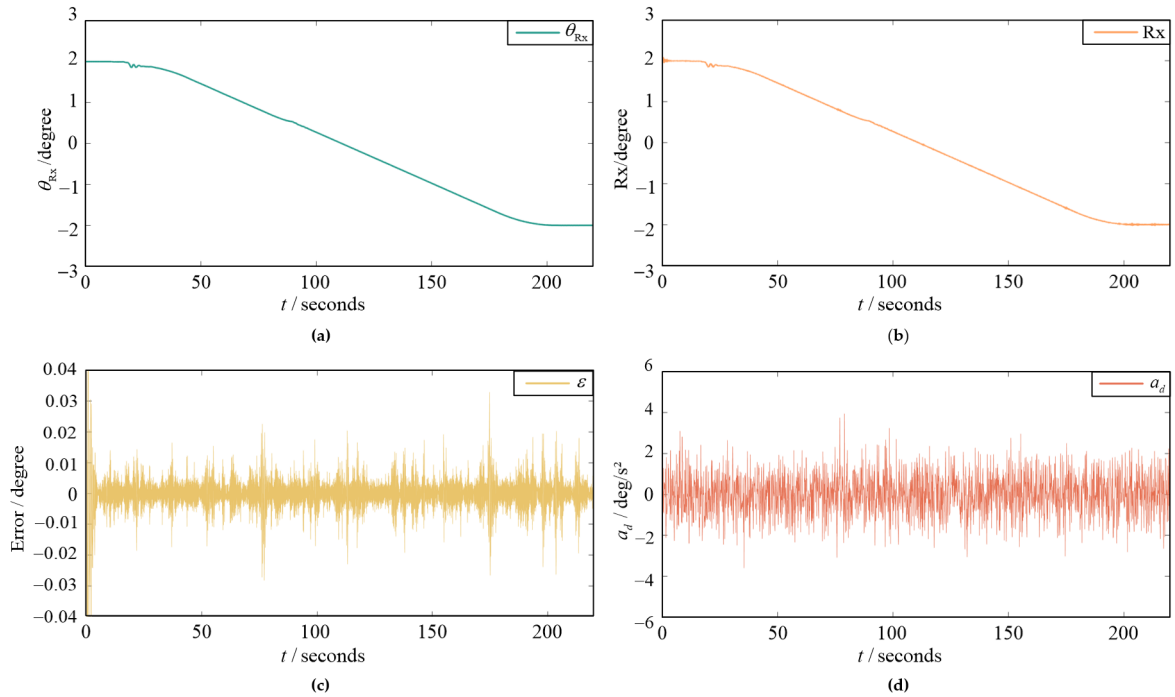


Figure 14. Conventional Attitude Setting Test Results—Rx. (**a**) Input for the Rx target in conventional attitude setting. (**b**) The Rx output attitude for conventional attitude setting. (**c**) Rx error in conventional attitude setting. (**d**) Disturbance acceleration.

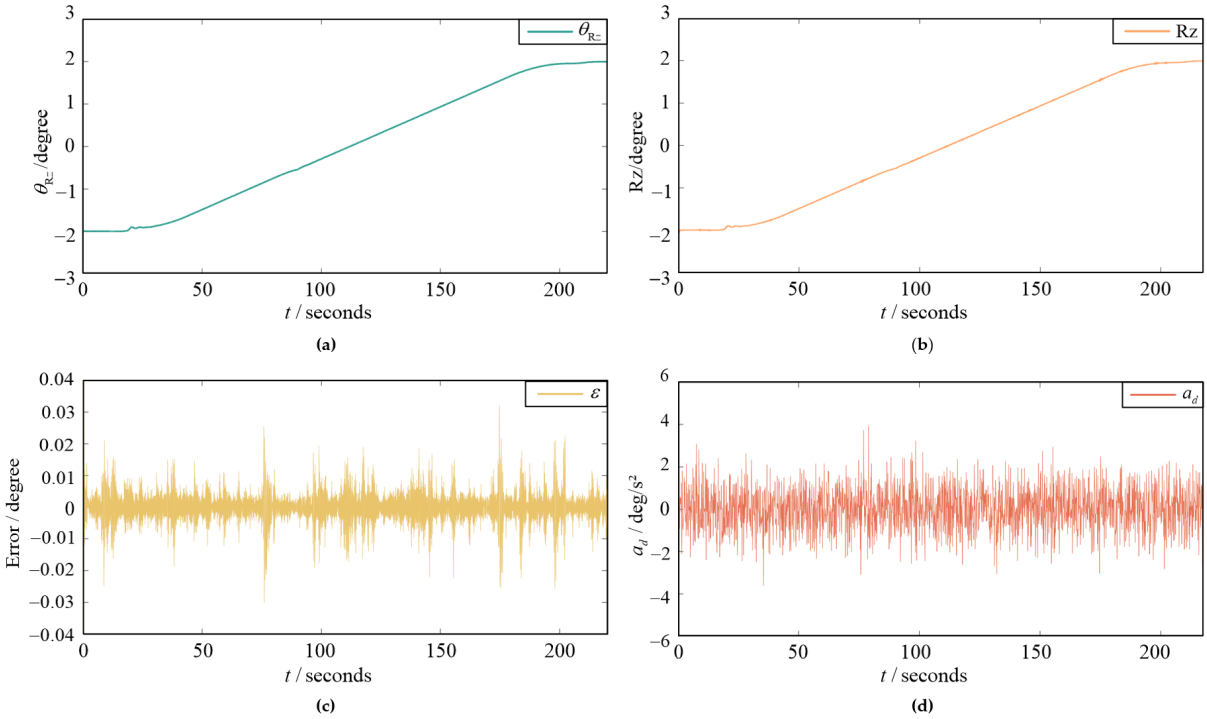


Figure 15. Conventional Attitude Setting Test Results—Rz. (**a**) Input for the Rz target in conventional attitude setting. (**b**) The Rz output attitude for conventional attitude setting. (**c**) Rz error in conventional attitude setting. (**d**) Disturbance acceleration.

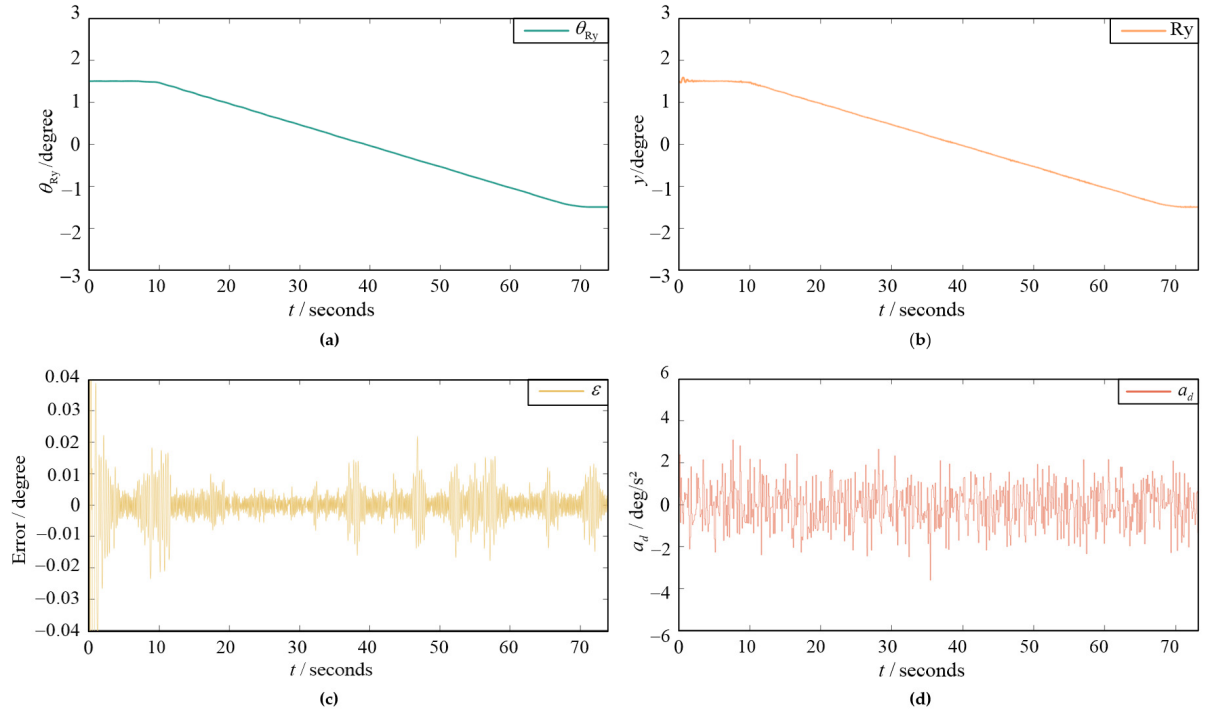


Figure 16. Conventional Attitude Setting Test Results—Ry. (**a**) Input for the Ry target in conventional attitude setting. (**b**) The Ry output attitude for conventional attitude setting. (**c**) Ry error in conventional attitude setting. (**d**) Disturbance acceleration.

The simulation results of conventional attitude setting scenarios demonstrate that the improved algorithm enables the spacecraft mock-up to be controlled with high precision and low loss through the dynamic adjustment of deadband thresholds and hysteresis width. The attitude angle converges within 3 s with no significant overshoot, and the

steady-state error stabilises at ±0.01 degrees. The operational data trends of the simulated curve demonstrate a high degree of correlation with those of the spacecraft model during routine attitude setting tests. This demonstrates its capability to meet the engineering requirements for long-term steady-state operation, as evidenced by the implementation of 'low redundancy manoeuvres' and 'high attitude retention accuracy'. Consequently, it establishes its position as a reliable solution for routine orbital attitude control.

5.3. Stability of the Attitude of the Simulated Connector in Separation Tests

The system parameter settings for maintaining the attitude stability of the simulated connector in the separation test are shown in Table 3.

Table 3. System parameters for maintaining the attitude stability of the simulated connector in separation tests.

System Parameters	Data	System Parameters	Data
h_0	0.1	β_{01}	−60
$e_{\max}$	0.01	β_{02}	−1000
θ_{D0}	0.001	β_{03}	−60
k_d	0.01	a_c	14
r	1		

The simulation results corresponding to this control system are presented in Figure 17.

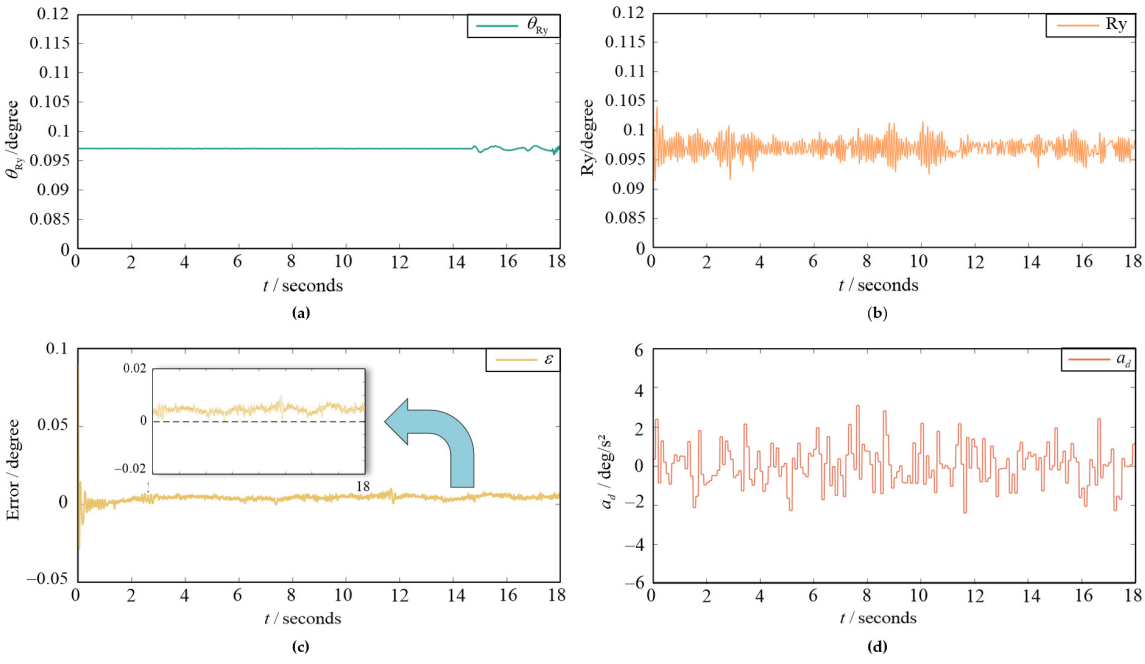


Figure 17. Yaw angle of the simulated connector in separation tests. (**a**) Simulated yaw input to the target in the separation test. (**b**) Yaw output of the simulated connector in separation tests. (**c**) Yaw error of the simulated connector in separation tests. (**d**) Disturbance acceleration.

In the attitude stabilisation scenario for the separation test connector, the core objective of the simulation is to validate the capability of the algorithm to maintain a stable yaw angle of the connector prior to separation. Therefore, the focus is on evaluating the improved algorithm's performance in suppressing minute disturbance torques and maintaining yaw angle stability before separation, using the actual yaw angle of the connector before separation in the ground full-physical experiment as the benchmark. The simulation results show that, during the entire pre-separation preparation phase, yaw angle fluctuations

caused by the improved algorithm remain within the range of ±0.01°. Compared to the original deadband–hysteresis controller, the improved algorithm demonstrates greater precision in maintaining yaw angle stability without inducing high-frequency oscillations in response to minor disturbances. This outcome shows that the enhanced algorithm can maintain precise alignment of the connecting body's yaw angle with the experimental reference value. This is achieved by estimating persistent minor disturbances prior to separation using an NESO, while dynamically adjusting the deadband threshold and hysteresis width. Yaw angle stability before separation is essential for the precise execution of subsequent manoeuvres. Thus, this simulation outcome directly validates the utility of the algorithm during critical preparatory stages of separation trials by resolving the engineering risk of attitude drift caused by minute disturbances that previously affected the original controller prior to separation.

5.4. Establishment of Initial Conditions in Docking Experiments

The system parameter settings for establishing initial conditions in the docking experiment are shown in Table 4.

Table 4. System parameters established for initial conditions in the docking experiment.

System Parameters	Data	System Parameters	Data
h_0	0.1	β_{01}	−40
$e_{\max}$	0.01	β_{02}	−1000
θ_{D0}	0.001	β_{03}	−40
k_d	0.01	a_c	10
r	0.5		

The simulation results corresponding to this control system are presented in Figure 18.

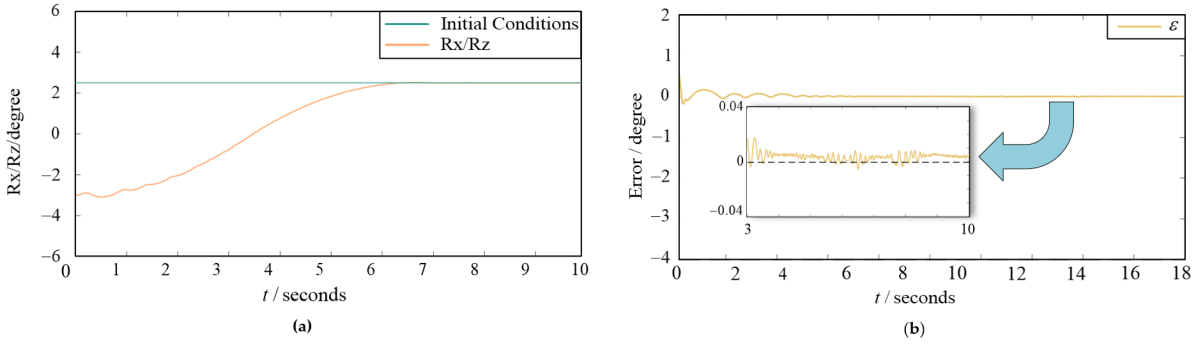


Figure 18. Results of establishing initial conditions in the docking experiment. (**a**) Initial conditions for Rx and Rz to be established for the docking experiment. (**b**) Establishing systematic errors in the initial conditions of the alignment experiment.

For establishing initial conditions in docking experiments, the improved algorithm achieves rapid convergence with high-precision attitude adjustment through the non-overshoot transition characteristics of the NTD and dynamic hysteresis width regulation. The convergence time from initial zero position to target attitude is merely 3 s, with no overshoot whatsoever. The final attitude error is controlled within ±0.01°, meeting the stringent requirements of millimetre-level precision and second-level response for initial attitude in docking tasks. Simulation plots demonstrate that the rotational or pitch angles of the aerospace mock-up rapidly and accurately transition from initial position to predetermined docking conditions, indicating its potential for high-precision, rapid attitude adjustment tasks in future engineering applications.

In summary, the enhanced controller employs a triple-innovation design comprising 'NTD optimisation of command response, NESO active compensation for total disturbances, and dynamic parameter adjustment for operational condition adaptation'. This approach comprehensively resolves the inherent shortcomings of the original deadband–hysteresis controller, namely 'low steady-state accuracy, weak disturbance rejection capability, and poor parameter adaptability'. The high correlation between simulation results and ground-based full-physical test data suggests that this algorithm holds promise for future practical engineering applications. It shows adaptability to diverse operational scenarios—including routine operation of the analogue unit, pre-separation attitude stabilisation, and initial condition establishment during docking—while remaining consistent with the engineering logic validated through ground experiments. This provides a valuable foundation and data support for the potential subsequent model-based application and in-orbit deployment of spacecraft attitude control algorithms.

6. Conclusions

The present paper addresses the attitude control requirements in ground-based full-physical experiments for spatial docking performance. The objective of this study is to address the fundamental limitations of conventional deadband–hysteresis relay controllers, namely low steady-state accuracy, inadequate disturbance rejection capability, and limited parameter adaptability, by proposing an enhanced algorithm based on ADRC. The innovation lies in the deep integration of ADRC's 'self-disturbance rejection' characteristics with the 'nonlinear switching' advantages of hysteresis, manifested as follows: Firstly, a dynamic adaptive logic for deadband and hysteresis parameters has been designed. The aforementioned factors enable real-time adjustment based on disturbance estimation and error magnitude, thereby resolving the contradiction in traditional controllers where 'deadband becomes redundant under weak disturbances yet insufficient under strong disturbances'. Secondly, the construction of an NESO incorporating a fault function to expand total disturbances into new state variables for real-time estimation and compensation, mechanistically overcomes control failure under strong disturbances. Thirdly, the introduction of NTD to orchestrate overshoot-free transitions resolves overshoot issues in step responses. The simulation results demonstrate that the enhanced algorithm demonstrates a high degree of consistency with ground-based full-physical experiment data for spacecraft docking performance. A conventional attitude setting is characterised by steady-state error remaining within $\pm 0.01^{\circ}$. It has been demonstrated that, prior to separation, the yaw angle of the connecting body is maintained at a stable level. During the initial condition establishment process for docking, convergence time is observed to be no greater than 3 s, with no occurrence of overshoot. At the simulation level, it has been demonstrated to fully satisfy core performance metrics, thus indicating excellent engineering application potential.

This paper provides a theoretical exposition of the motion characteristics and parameter sensitivity of traditional controllers. Employing the phase plane method, this paper systematically reveals these characteristics. Under the standard assumption of bounded disturbance change rates, the present study refines the stability analysis framework for nonlinear attitude control. It should be noted that the stability analysis of the NESO is conducted under this standard assumption, while a comprehensive theoretical framework capable of rigorously accommodating non-Lipschitz disturbances, such as Coulomb friction jumps, remains an important topic for future research. At the engineering validation level, the simulation results demonstrate the potential of the proposed enhanced ADRC framework in ground-based experimental setups simulating spacecraft mass–inertia characteristics, indicating a promising yet preliminary stage of research. Nevertheless, several clear limitations persist: the validation has not yet encompassed extreme in-orbit condi-

tions or full-spectrum disturbance environments; parameter tuning remains empirically dependent; and, most critically, the lack of HIL validation represents a key gap in assessing the algorithm's adaptability to real-world engineering factors such as sensor quantization and actuator saturation. Furthermore, the current study focuses on validating the performance potential of the proposed framework, while the computational load associated with the NESO—involving multiple state variables and nonlinear function evaluations—would require dedicated optimisation for implementation on resource-constrained embedded systems. Consequently, the current outcomes should be regarded as promising but preliminary. Subsequent work will prioritise the establishment of a semi-physical simulation platform for HIL testing, along with the development of automated parameter tuning tools and the investigation of computationally efficient implementations (e.g., simplified NESO variants or fixed-point arithmetic), to advance this framework from simulation validation toward future engineering implementation and to ensure its feasibility in resource-aware applications.

Author Contributions: Conceptualization, X.Z. and Y.T.; methodology, X.Z. and Y.T.; software, Y.T.; validation, X.Z. and Y.T.; formal analysis, Z.J., Z.X. and M.L.; investigation, X.B.; resources, Z.J. and Z.X.; data curation, M.L. and X.B.; writing—original draft preparation, X.Z. and Y.T.; writing—review and editing, X.Z. and Y.T.; supervision, Z.J. and Z.X.; project administration, Z.X., M.L. and X.B.; funding acquisition, Z.J. and Z.X. All authors have read and agreed to the published version of the manuscript.

Funding: This research was funded in part by the NSFC under Grant 52575012; in part by the Liaoning Provincial Natural Science Foundation under Grant 2025-MS-084; and in part by the Youth Program of the Basic Research Plan, Shenyang Institute of Automation, Chinese Academy of Sciences under Grant 2023JC1K11.

Data Availability Statement: Data is contained within the article.

Conflicts of Interest: The authors declare no conflicts of interest.

Abbreviations

The following abbreviations are used in this manuscript:

ADRC	Auto disturbance rejection control
NESO	Nonlinear extended state observer
NTD	Nonlinear tracking differentiator
DDPG	Deep deterministic policy gradient
ESO	Extended state observer
DOF	Degree of freedom
HIL	Hardware-in-the-loop

References

1. Zhou, J.P. Rendezvous and Docking Technology of Manned Space Flight. *Manned Spacefl.* **2011**, *17*, 1–8. [CrossRef]
2. Jin, F.W. Analysis and Experimental Research of Docking Mechanism Test-Bed System. Master's Thesis, Harbin Institute of Technology, Harbin, China, 2006.
3. Zhang, H.; Xiao, Y.Z.; Xu, B.H.; Tao, W.M. Analysis Study on Separation of Aerospace Vehicle and Ground Simulation Test. *J. Astronaut.* **2008**, *29*, 1761–1765.
4. Su, L.; Shi, Y.; Zhang, Z.H.; Liu, Y.; Peng, H.K. The ground test method for spacecraft rendezvous and docking. *Spacecr. Environ. Eng.* **2014**, *31*, 277–282.
5. Wang, Z.; Yu, Y.Y.; Jin, X.L.; Xu, Z.F.; Gao, Z.G.; Yang, N.; Liu, L.L. Data and Knowledge Fusion-driven Digital Twin Experiment for Space Docking Mechanisms. *Aerosp. Shanghai (Chin. Engl.)* **2025**, *42*, 144–156+176. [CrossRef]
6. Peng, L.K.; Wang, C.Y.; Lv, B.J.; Chen, J.; Huang, B.; Pan, W. Review on key technologies of ship maneuvering simulator based on motion platform. *Ship Sci. Technol.* **2025**, *47*, 1–6.

7. Zhao, S.Q.; Peng, F.Y.; Su, J.T.; Sun, H.; Yan, R.; Tang, X.W.; Zhang, T.; Li, Z.P. A self-adaptive agent for flexible posture planning in robotic milling system. *J. Manuf. Syst.* **2024**, *75*, 228–245. [CrossRef]
8. Yan, K.; Ma, B.L. A unified controller of global trajectory tracking and posture regulation for a car-like mobile robot. *Int. J. Robust Nonlinear Control* **2024**, *34*, 8590–8604. [CrossRef]
9. Khan, S.A.; Shiyou, Y.; Ali, A.; Rao, S.W.; Fahad, S.; Jing, W.; Tong, J.J.; Tahir, M. Active attitude control for microspacecraft; A survey and new embedded designs. *Adv. Space Res.* **2022**, *69*, 3741–3769. [CrossRef]
10. Zuo, H.W.; Shen, Q.; Ouyang, S.R.; Razoumny, V.Y.; Razoumny, Y.N.; Wu, S.F. Adaptive fault-tolerant attitude control on SO(3) under multiple attitude constraints and finite sequential actuator faults. *Acta Astronaut.* **2025**, *228*, 370–383. [CrossRef]
11. Zhang, S.X.; Liu, Y.H.; Hu, X.R.; Zheng, L.M.; Zheng, S.Y. Fully Informed Fuzzy Logic System Assisted Adaptive Differential Evolution Algorithm for Noisy Optimization. *IEEE Trans. Fuzzy Syst.* **2025**, *33*, 1876–1888. [CrossRef]
12. Reza, M.K.; Prater-Bennette, A.; Asif, M.S. Robust Multimodal Learning With Missing Modalities via Parameter-Efficient Adaptation. *IEEE Trans. Pattern Anal. Mach. Intell.* **2025**, *47*, 742–754. [CrossRef] [PubMed]
13. Faraji, B.; Gheisarnejad, M.; Yalsavar, M.; Khooban, M.H. An Adaptive ADRC Control for Parkinsons Patients Using Machine Learning. *IEEE Sens. J.* **2021**, *21*, 8670–8678. [CrossRef]
14. Peng, L.H.; Xiong, X.Y.; Wang, L.J. Research on yarn tension control technology for knitting underwear machine based on adaptive ADRC. *Sci. Rep.* **2025**, *15*, 9750. [CrossRef] [PubMed]
15. Han, J.Q. Auto Disturbances Rejection Control Technique. *Front. Sci.* **2007**, *1*, 24–31.
16. Gao, Z.Q. Scaling and bandwidth-parameterization based controller tuning. In Proceedings of the Annual American Control Conference (ACC 2003), Denver, CO, USA, 4 June 2003; pp. 4989–4996.
17. Stankovic, M.; Ting, H.; Madonski, R. From PID to ADRC and back: Expressing error-based active disturbance rejection control schemes as standard industrial 1DOF and 2DOF controllers. *Asian J. Control* **2024**, *26*, 2796–2806. [CrossRef]
18. Li, Z.G.; Liang, S.; Guo, M.M.; Zhang, H.; Wang, H.; Li, Z.B.; Li, H.Y. ADRC-Based Underwater Navigation Control and Parameter Tuning of an Amphibious Multirotor Vehicle. *IEEE J. Ocean. Eng.* **2024**, *49*, 775–792. [CrossRef]
19. Zhang, P.; Shi, Z.Y.; Yu, B.; Qi, H.J. Research on a Sensorless ADRC Vector Control Method for a Permanent Magnet Synchronous Motor Based on the Luenberger Observer. *Processes* **2024**, *12*, 906. [CrossRef]
20. Li, J.; Lu, Y.; He, J.R.; Xie, P.Y.; Li, Y.W. Overshoot Suppression of Hydraulic Actuation Based on the Integrating Flow Compensation: Applied to Lift Tracking Control of an Engine Variable Valve Actuator. *IEEE Trans. Autom. Sci. Eng.* **2025**, *22*, 21686–21700. [CrossRef]
21. Zhang, R.X.; Yang, R.; Jia, F.H.; Chang, F.; Zhao, W.; Yao, Y.T.; Lin, G.C.; Zhang, X.L.; Yuan, W.J.; Liu, L.W. Working range extension and overshoot suppression strategies for flexible strain sensors based on a "Kirigami-Sensor-Kirigami" serial system with high conformability. *Sens. Actuators A Phys.* **2025**, *391*, 116570. [CrossRef]
22. Liu, C.Y.; Xiong, W.L. Multi-objective Optimization Control of Wastewater Treatment Process Based on Overshoot Suppression Strategy. *Inf. Control* **2024**, *53*, 250–260+272. [CrossRef]
23. Liu, Y.Z.; Chen, L.Q. *Nonlinear Vibration*; Higher Education Press: Beijing, China, 2001.

Disclaimer/Publisher's Note: The statements, opinions and data contained in all publications are solely those of the individual author(s) and contributor(s) and not of MDPI and/or the editor(s). MDPI and/or the editor(s) disclaim responsibility for any injury to people or property resulting from any ideas, methods, instructions or products referred to in the content.